

MoSi₂N₄-like crystals – the new family of two-dimensional materials

T. Latychevskaia¹, D. A. Bandurin^{2*}, K. S. Novoselov^{3*}

¹*Paul Scherrer Institute, Forschungsstrasse 111, 5232 Villigen, Switzerland*

²*Department of Materials Science and Engineering, National University of Singapore, Singapore, 117575, Singapore*

³*Institute for Functional Intelligent Materials, National University of Singapore, Building S9, 4 Science Drive 2, Singapore 117544*

*E-mail: dab@nus.edu.sg; kostya@nus.edu.sg

Abstract

Recently-synthesised MoSi₂N₄ is the first septuple layer two-dimensional material, which doesn't naturally occurs as a layered crystal, and has been obtained with CVD growth. It can be considered as MoN₂ crystal (with a crystal structure of MoS₂) intercalating Si₂N₂ two-dimensional layer (with the structure similar to InSe). Such classification gave rise to the understanding of the electronic properties of the material, but also to the prediction of other members of the family (many dozens of them) as well as to the way to classify those. Whereas the originally-synthesised MoSi₂N₄ is a semiconductor, some of the members of the family are also metallic and some even demonstrate magnetic properties. Interestingly, the room-temperature mobility predicted for such crystals can be as high few thousands cm²/V·s (hole mobility typically higher than electron) with some record cases as high as 5×10⁴ cm²/V·s, making these materials strong contenders for future electronic applications. The major interest towards these materials is coming from the septuple layer structure, which allows multiple crystal phases, but also complex compositions, in particular those with broken mirror-reflection symmetry against the layer of metal atoms.

Contents

1	Introduction	2
2	Synthesis and experimental characterization	4
3	Universal structure of the family.....	4
3.1	Symmetry consideration for MA_2Z_4	4
3.2	Related structures – Janus crystals	6
3.3	Related structures - $MoSi_2N_4(MoN)_4$	6
4	Mechanical properties	7
5	Thermal conductivity and thermoelectric properties.....	8
6	Band structure.....	8
7	Magnetic Properties	9
8	Valley properties	10
8.1	Berryology and valley-contrasting phenomena in MA_2Z_4 family	10
8.2	Spin-valley splitting	10
8.3	Valley-contrasting effects.....	11
9	Transport Properties.....	12
10	Topological properties	14
11	Optical properties	15
12	Heterostructures.....	17
13	Catalytic properties.....	19
14	Conclusions.....	22

1 Introduction

For many years there was a dogmatic approach in the field of two-dimensional (2D) materials that such one atom thick objects need to be originally present as layers in a van der Waals crystal. Indeed, a large number of 2D materials have been obtained by micromechanical^{1,2} (Novoselov2004Science, Novoselov2005PNAS) or liquid phase exfoliation³ (Nicolosi2013Science). The most prominent example is graphene obtained by mechanical exfoliation from graphite. Later, other established chemical synthesis methods: chemical vapor deposition (CVD), etching, as well as various epitaxial techniques, were employed to produce such one-atom thick fabrics^{4,5} (Bhimanapati2015ACSNano, Cai2018ChemRev). By using etching method, for example, new 2D materials – the 2D transition metal carbides (MXenes) and 2D transition metal borides (MBenes) – have been synthesized⁶⁻¹² (Naguib2011AdvMat, Naguib2012ACSNano, Naguib2014AdvMat, Guo2017JMatChemA, Zhang2018JMatSciTech, Alameda2018JAmChemSoc, Zhang2022JMatChemA). MAX materials (M is a transition metal element, A is an element from group 13 or 14 and X is either

carbon or nitrogen) are the three-dimensional (3D) precursor to MXenes, they have a layered structure where $M_{n+1}X_n$ layers are separated by A-layers. Because of relatively weak M-A bonds, the A layers are selectively etched away, leaving 2D MXenes nano-sheets. However, until recently, there were no examples of 2D materials without a layered 3D counterpart – it is not even clear how such materials can be created, as neither exfoliation, nor selective etching would work here.

And yet, a few years ago the first 2D material without 3D counterpart was synthesised^{13,14} (Hong2020Science, Novoselov2020NatSciRev). Researchers managed to passivate the surface of monolayer MoN_2 with silicon, thus quenching the growth at the monolayer stage, and creating a 2D material of a composition $MoSi_2N_4$, with septuple atomic layers arranged as N-Si-N-Mo-N-Si-N, Fig. 1. The complex layered structure as well as the multiple possibilities for substitutions for all three elements give rise to a new family of 2D materials, very rich in compositions as well as in crystal phases. So far only two members of the family have been experimentally synthesised so far ($MoSi_2N_4$ and WSi_2N_4)¹³ (Hong2020Science), but the overall strategy for the growth of such crystals is clear and there is no doubt that more of the members of the family will be obtained experimentally in the very near future. In the following we will categorize the multiple possible members of this family, and review their most exciting physical and chemical properties.

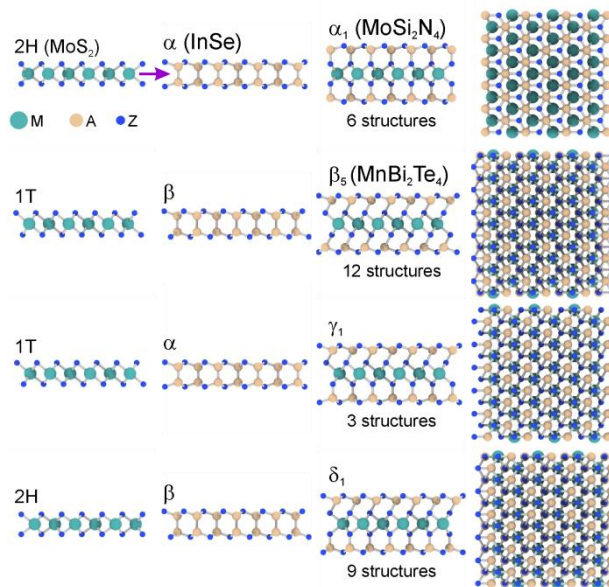


Fig. 1. Structure of $MoSi_2N_4$ family. Four symmetry types of MA_2Z_4 structures, characterised based on the symmetry of the parent $MoSi_2$ and $InSe$ structures. The structures are drawn using the data provided in ref. 15.

No.	phase	symmetry group	$a / \text{\AA}$
1	α_1	$P\bar{6}m2$	2.909
2	α_2	$P\bar{6}m2$	2.901
3	α_3	$P\bar{6}m2$	2.835

4	α_4	P $\bar{6}$ m2	2.842
5	α_5	P $\bar{6}$ m2	2.864
6	α_6	P $\bar{6}$ m2	2.845
7	β_1	P $\bar{3}$ m1	2.909
8	β_2	P $\bar{3}$ m1	2.921
9	β_3	P $\bar{3}$ m1	2.874
10	β_4	P $\bar{3}$ m1	2.857
11	β_5	P $\bar{3}$ m1	2.842
12	β_6	P $\bar{3}$ m1	2.841
13	β_7	P $\bar{3}$ m1	2.900
14	β_8	P $\bar{3}$ m1	2.933
15	β_9	P $\bar{3}$ m1	2.878
16	β_{10}	P $\bar{3}$ m1	2.853
17	β_{11}	P $\bar{3}$ m1	2.876
18	β_{12}	P $\bar{3}$ m1	2.859
19	γ_1	P3m1	2.882
20	γ_2	P3m1	2.872
21	γ_3	P3m1	2.868
22	δ_1	P3m1	2.871
23	δ_2	P3m1	2.872
24	δ_3	P3m1	2.854
25	δ_4	P3m1	2.905
26	δ_5	P3m1	2.839
27	δ_6	P3m1	2.888
28	δ_7	P3m1	2.854
29	δ_8	P3m1	2.841
30	δ_9	P3m1	2.875

Table 1. Structural properties of 30 MA₂Z₄ monolayer candidates. a is the in-plane lattice constant. xy represent the x and y coordinates of the atomic positions in the order of N1-N2-N3-N4-Mo1-Si1-Si2. a, b and c represent the sites in trigonal lattice. $z_{N1}, z_{N2}, z_{N3}, z_{N4}, z_{Mo1}, z_{Si1}$ and z_{Si2} are the fractional z- coordinate the atomic positions; the z-axis unit cell is 30 Å. Adapted with permission from ref. 15.

2 Synthesis and experimental characterization

In order to synthesize MoSi₂N₄ crystals, a sandwich of Mo and Cu foils was exposed to NH₃ gas as nitrogen source, and a pure silicon (or quartz) plate was placed either upstream or directly above the copper foil as a silicon source. The growth temperature was 1080°C. In the absence of the silicon supply – only nanocrystals of non-layered Mo₂N of approximately 10 nm in thickness were grown. Addition of silicon resulted in fairly large, triangular domains of MoSi₂N₄, which could fuse into a continuous film upon further growth. TEM analysis confirmed the septuple layer structure.

3 Universal structure of the family

3.1 Symmetry consideration for MA₂Z₄

The first septuple layer 2D material – MnBi₂Te₄ – was synthesized in 2013¹⁶ (Lee2013 Crystengcomm) and later intensively studied for its magnetic and topological properties¹⁷⁻²³

(Gong2015ChinPhysLett, Peng2019PRB, Li2019SciAdv, Zhang2019PRL, Otrokov2019PRL, Deng2020Science, Gao2021Nature). However, only with the appearance of the MoSi_2N_4 it was realized that such crystals compose a whole new class of materials. In order to classify the possible structures, the easiest way is to think about such materials not as MoN_2 layer passivated with silicon (even though this way of thinking helps when studying the synthesis process), but rather as a MoN_2 layer (with a structure similar to that of, for instance MoS_2 transition metal dichalcogenide (TMD)) intercalating Si_2N_2 , where single SiN layer has a structure similar to that of InSe .

In more general terms, a MA_2Z_4 monolayer can be constructed by intercalation of a MZ_2 layer into a A_2Z_2 layer (MZ_2 layer is sandwiched between AZ layers, Fig. 1)¹⁵ (Wang2021NatCommun). Here M can stand for elements of transition metal groups IVB, VB and VIB; A – for Si or Ge ; and Z – for N , P or As . The further classification originates from the fact, that a MZ_2 monolayer can exist in 2H or 1T high symmetry phase and a A_2Z_2 monolayer – in α or β phases. Thus, an MA_2Z_4 2D crystal structure is given by combination of one of the phases of MZ_2 monolayer with one of the phases of A_2Z_2 monolayer. Each side of MZ_2 has three high-symmetry location sites for A and Z atoms in AZ layer, thus making 6 possible structural arrangements. Because the arrangement of AZ layers on two sides of MZ_2 can be different, this gives in total 36 different configurations for each pair of MZ_2 and A_2Z_2 monolayers. Moreover, there are 144 possible configurations when considering combinations of 2H or 1T phases of MZ_2 with either α or β phases of A_2Z_2 . It has been shown¹⁵ (Wang2021NatCommun), that only 39 of those configurations are original – the others are related via symmetry transformations. Only 30 of them are found to be stable (Table 1), and they are split into four groups: α (6 structures), β (12 structures), γ (3 structures) and δ (9 structures), shown in Fig. S1. Calculations demonstrate that it is the β_5 phase which has the lowest energy^{21,22,24,25} (Otrokov2019PRL, Otrokov2019Nature, Deng2020Science, He2020npjQuanMat) for MnBi_2Te_4 , and α_1 phase for MoSi_2N_4 and WSi_2N_4 , as indeed has been observed in the experiments¹³ (Hong2020Science).

To classify the MA_2Z_4 compounds even further, it is important to consider the number of valence electrons¹⁵ (Wang2021NatCommun). Thus, it is the β_2 phase which has the lowest energy for crystals with 32 electrons where M belongs to transition metal groups IVB, VB or VIB, $\text{A}=\text{Si}$ or Ge , and Z is N , P , or As . Different situation is found for the 33 and 34 valence electrons compounds. It is the α_1 phase which has the lowest energy for MSi_2N_4 (where M is V , Nb , Ta , Cr , Mo , W), MGe_2N_4 (for $\text{M}=\text{Nb}$, Ta , Mo , W) and MSi_2P_4 ($\text{M}=\text{Nb}$, Ta – 33 electron systems); and α_2 phase for MSi_2P_4 ($\text{M}=\text{Cr}$, Mo , W – 34 electron systems), MGe_2P_4 ($\text{M}=\text{V}$, Nb , Ta , Cr , Mo , W), MSi_2As_4 ($\text{M}=\text{V}$, Nb , Ta , Mo , W) and MGe_2As_4 ($\text{M}=\text{V}$, Nb , Ta , Mo , W). The monolayers where the metal atom is either from the alkali-earth group or group IIB are found to be either in β_1 or β_2 phase.

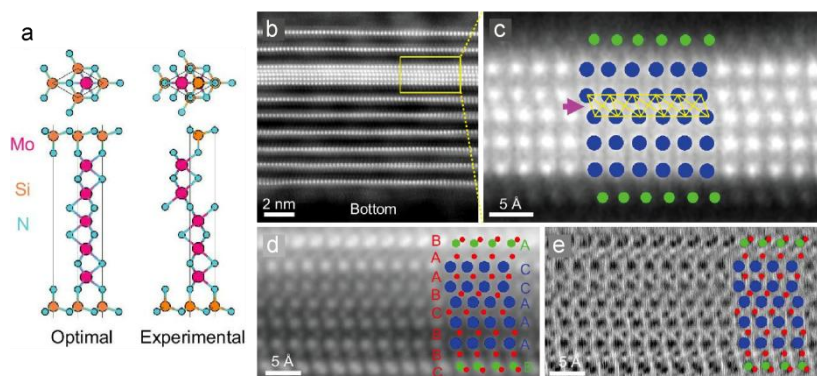


Fig. 2. Transmission electron microscopy study of $\text{MoSi}_2\text{N}_4(\text{MoN})_4$. **a**, The atomic models of the energetically favourable and experimental structure of $\text{MoSi}_2\text{N}_4(\text{MoN})_4$. **b – c**, high-angle annular dark-field imaging scanning transmission electron microscopy (HAADF-STEM) image of $\text{MoSi}_2\text{N}_4(\text{MoN})_4$ confined in multilayer MoSi_2N_4 (**b**) and the zoomed-in view of the $\text{MoSi}_2\text{N}_4(\text{MoN})_4$ (**c**). **d – e**, integrated differential phase contrast (iDPC) (**d**) and differentiated differential phase contrast (dDPC) (**e**) images of $\text{MoSi}_2\text{N}_4(\text{MoN})_4$. The blue, green and red balls represent the Mo, Si and N atoms, respectively. Reproduced with permission from ref. ²⁶.

3.2 Related structures – Janus crystals

The layer structure of MA_2Z_4 materials makes it possible to create the so-called Janus structures that lacks the inversion symmetry with respect to the plane passing through the middle atomic layer (for instance - molybdenum). Such Janus structures have been previously studied both theoretically and experimentally²⁷ (Zhang2020JMaterChem). Potentially, materials like MoSiGeN_4 (as well as many other materials of the family MABZ_4) can be synthesized simply by adding not only Si, but also Ge during the growth process. However, the experimental conditions which would lead to elemental separation according to the layers are yet to be explored.

Indeed, many Janus structures of the MABZ_4 family have been found²⁸⁻³⁰ (Guo2021JMaterChem2464, Yu2021ACS, Guo2021JMtChem7465) stable through the DFT calculations: MoSiGeN_4 , WSiGeN_4 , SrAlGeSe_4 and others. Interestingly, the calculations indeed confirm separation of the elements between the layers. The peculiar feature of the Janus materials is the possibility of existence of the intrinsic out-of-plane electric field. Such field can induce the Rashba spin splitting around the Γ point, as indeed has been seen in the calculations³⁰ (Guo2021JMatChemC) for both MoSiGeN_4 , WSiGeN_4 . This provides a complex spin texture in x-y plane, with no z component of the spin.

3.3 Related structures - $\text{MoSi}_2\text{N}_4(\text{MoN})_4$

The intercalation analogy can be taken further. It has been demonstrated²⁶ (Liu2023NatSciRev) that increase of the flux of NH_3 during the growth creates more MoN layers intercalated between SiN layers, Fig. 2. The generic formula of the resulting compound is $\text{MoSi}_2\text{N}_4(\text{MoN})_{4n}$, where $n=0, 1, 2, 3, \dots$. Thus, the $\text{MoSi}_2\text{N}_4(\text{MoN})_4$ compound ($n=1$) can be seen as 5 layers of MoN (Mo_5N_6) sandwiched

between two SiN layers. Thicker samples with n up to 10 have also been observed in the experiment. Interestingly, experimentally obtained $\text{MoSi}_2\text{N}_4(\text{MoN})_4$ crystals demonstrate a Mo octahedral stacking fault, even though theory predicts that the perfect structure (which contains only the MoN triangular prisms) has an energy, which is 108 meV lower than the one with the stacking fault. Density functional theory (DFT) calculations suggest²⁶ (Liu2023NatSciRev) that unlike MoSi_2N_4 (which is a semiconductor) – the thicker $\text{MoSi}_2\text{N}_4(\text{MoN})_4$ compound is metallic. Moreover, it has been predicted that it can be a phonon-mediated superconductor with the critical temperature of 9.02 K.

4 Mechanical properties

The mechanical properties of MoSi_2N_4 crystals have been measured experimentally via atomic force microscopy (AFM) nanoindentation¹³ (Hong2020Science). The Young modulus and the breaking strength were found to be 491.4 ± 139.1 GPa and 65.8 ± 18.3 GPa respectively; the numbers confirmed with DFT calculations³¹ (Li2022PhysicaE). The origin of such relatively high Young modulus was understood once comparing the mechanical properties of MoSi_2N_4 and $\text{MoSi}_2\text{N}_4(\text{MoN})_{4n}$ compounds. It has been observed that the MoSi_2N_4 has much higher Young modulus than crystals that contain $\text{Mo}_{n+1}\text{N}_{n+2}$ layers, and the Young modulus of $\text{MoSi}_2\text{N}_4(\text{MoN})_{4n}$ changes only slightly with the number of MoN layers²⁶ (Liu2023NatSciRev). This suggests that the major contribution to the higher Young modulus is mainly provided by the SiN layers, which can be explained by ionic nature of Si-N bonds, compared to more covalent Mo-N.

Some of the phases of MA_2Z_4 compounds demonstrate the lack of inversion symmetry and thus can possess piezoelectric properties. Thus, the α phases belong to the $P\bar{6}m2$ group (no inversion symmetry), thus exhibiting piezoelectric properties and the β phases belong to the $P\bar{3}m1$ group – preserving such symmetry³² (Guo2021CompMatSci). The piezoelectric properties have been calculated by many authors for a number of different semiconducting MA_2Z_4 compounds³⁰⁻³⁴ (Guo2021JMaterChem7465, Li2021PhysicaE, Guo2021CompMatSci, Bafekry2021JPhysD, Mortazavi2021NanoEnergy). For α_1 - MoSi_2N_4 and α_1 - WSi_2N_4 (which have been experimentally synthesized) the in-plane piezoelectric strain d_{11} are 1.14 pm/V and 0.78 pm/V respectively³² (Guo2021CompMatSci). These values are somewhat smaller than those found in 2D TMD semiconductors^{35,36} (Blonsky2015ACSNano, Duerloo2012JPhysChem), mainly due to large in-plane stiffness. Among other possible compounds, those based on phosphorous predicted³² (Guo2021CompMatSci) to have significantly higher d_{11} , for instance 4.91 pm/V for α_1 - MoSi_2P_4 and 6.12 pm/V for α_1 - CrGe_2P_4 .

Sliding ferroelectricity is an exciting phenomenon, observed in multilayer van der Waals heterostructures^{37,38} (Geim2013Nature, Novoselov2016Science) where certain stacking results in local breaking of the vertical inversion symmetry³⁹⁻⁴¹ (Woods2021NatCommun,

ViznerStern2021Science, Weston2022NatNanotech). Similarly, the relatively low symmetry of MA_2Z_4 compounds offer bilayer stacking configurations with strong ferroelectric domains. Thus, vertical polarisations can be⁴² (Zhong2021JMatChemA) as high as 3.36 pC/m and 3.05 pC/m for $MoSi_2N_4$ and $MoGe_2N_4$, and 2.49 pC/m and 3.44 pC/m for $CrSi_2N_4$ and WSi_2N_4 , respectively, which is significantly higher than, for instance for bilayer WTe_2 (predicted⁴³ (Yang2018JPhysChemLett) to be ~ 0.37 pC/m).

5 Thermal conductivity and thermoelectric properties

The large in-plane stiffness – being detrimental for piezoelectric properties of MA_2Z_4 compounds – can be beneficial for their thermal conductivity. The phonon spectra of such compounds consist of 3 acoustic branches and 18 optical branches⁴⁴ (Yin2021ASC) with the acoustic phonons contributing the most to the thermal conductivity (typically of the order of 75%)³⁴ (Mortazavi2021NanoEnergy). The important parameter determining the thermal conductivity is the phonon group velocity, which by itself depends on the width of the dispersion of a particular phonon band (the wider the band – the higher the group velocity). It turns out that the width of the phonon bands depends strongly on the A and Z atoms, but only marginally on the M atom³⁴ (Mortazavi2021NanoEnergy). Thus, it has been predicted that room temperature thermal conductivity for $MoSi_2N_4$ and WSi_2N_4 are 439 W/m·K and 503 W/m·K respectively (though lower values can also be found in literature^{45,46} (Yu2021NewJPhys, Zhang2022JSolidState)), but drops by a factor of 4 if nitrogen is replaced with phosphorous. Thermal conductivity is found to decay with temperature as $1/T$, suggesting the Umklapp phonon scattering as the dominant scattering mechanism^{45,46} (Yu2021NewJPhys, Zhang2022JSolidState). Interestingly, thermal conductivity is not sensitive for the choice of the M atom if they belong to the same group⁴⁴ (Yin2021ASC). At the same time, as the bond-strength depends on the valence of the M atom – the thermal conductivity changes significantly depending on to which group in the periodic table the M atom belongs to.

The high thermal conductivity would reduce the efficiency of the thermoelectric effect in such materials. The figure of merit for $MoSi_2N_4$ at room temperatures has been predicted to be of the order of 0.05, though increasing with temperature due to decrease of the thermal conductivity.

6 Band structure

The band structure of MA_2Z_4 compounds strongly depends on the number of valence electrons. Thus, MA_2N_4 compounds (nitrides) with 32 electrons are found to be semiconductors¹⁵ (Wang2021NatCommun). At the same time, MA_2P_4 compounds (phosphides) and MA_2As_4 (arsenides) with the same number of electrons predicted to be metallic. This is due to the fact that the hybridization between the M atom and phosphorous or arsenic is much weaker than between M atom and nitrogen.

Most of the 34 electron systems are semiconductors (which indeed has been experimentally confirmed for MoSi_2N_4 , which has been confirmed as a semiconductor¹³ (Hong2020Science)), and only CrGe_2N_4 , CrSi_2As_4 , CrGe_2As_4 are predicted to be metallic ferromagnets¹⁵ (Wang2021NatCommun). Many of the systems with 33 electrons exhibit ferromagnetic properties, and those which don't are typically metallic, since the unpaired electron would give rise to a half-filled band.

7 Magnetic Properties

Among the variety of 2D materials, only a few exhibit magnetism in a 2D limit. The emergent family of MA_2Z_4 materials promises to change this situation as they were predicted to feature diverse, intrinsic magnetic properties even in the monolayer form. The freedom of arranging three different elements in a seven-layered crystal structure makes MA_2Z_4 materials rich with various physical properties, including magnetism. Generally, the M atoms of MA_2Z_4 nano-sheets (M = V, Nb, or Ta) are responsible for the ferromagnetic states as the magnetic moments are found to be localized on the d orbital of M-atoms^{47,48} (Zhao2023ApplSurfSci, Chen2021ChemA). When M is either V, Nb, or Ta atoms, MA_2Z_4 materials were predicted to exhibit a magnetic ground state and can be either ferromagnetic or antiferromagnetic in nature. V-based monolayer VA_2Z_4 materials are semiconducting ferromagnets whereas VGe_2N_4 are ferromagnetic half-metals with a magnetic moment of $1 \mu_B$ per metal atom (V)^{48,49} (Chen2021ChemA, Li2022NewJPhys). For example, the ground states of VSi_2Z_4 , VSi_2P_4 and VSi_2N_4 are ferromagnetic; these materials exhibit spin-gapless semiconducting properties, and can offer spin-filtering⁵⁰ (Feng2022APL). Magnetism, similarly to other properties of MA_2Z_4 materials, has been also predicted to be sensitive to strain. In particular, numerous phase changes are envisioned in MA_2Z_4 crystals: from compression-enabled suppression of magnetism to semiconductor-to-half-metal transitions under biaxial strain^{47,50} (Zhao2023ApplSurfSci, Feng2022APL). The presence of magnetic order in this new class of 2D materials may find its applications in the field of spintronics.

The magnetic moments in NbSi_2N_4 , VSi_2N_4 , and VSi_2P_4 are theoretically found to be aligned in-plane and, therefore, have easy magnetization with negligible magnetic anisotropy^{47,51} (Zhao2023ApplSurfSci, Akanda2021APL). The magnetic anisotropy energy is dependent on the metal atoms. An increase in strain in the ZnSi_2N_4 layer shows that it can change the magnetic anisotropy from perpendicular to in-plane magnetic anisotropy⁴⁷ (Zhao2023ApplSurfSci). These materials also display high Curie temperatures^{49,50} (Feng2022APL, Li2022NewJPhys). For VSi_2X_4 nanosheets, the Curie temperature is in the range of 230–250 K. For VGe_2N_4 , it is reported that the ferromagnetic phase is stable under strain (tensile or compressive), and the Curie temperature can reach 325 K, a value over room temperature, by the presence of compressive strain. The Curie temperature of

VSi_2N_4 is estimated to be around 507 K⁵¹ (Akanda2021APL). Overall, the value of Curie temperature is higher compared to the other 2D magnets like CrI_3 (45 K)⁵² (Huang2017Nature) or Fe_3GeTe_2 (130 K)⁵³ (Fei2018NatMater). The substitutional doping of transition metals can introduce alternate spin channels and induce magnetic moments in nonmagnetic MA_2Z_4 materials such as MoSi_2N_4 . Mn-doped MoSi_2N_4 is reported to exhibit spin-polarization up to 86% and has a potential for applications in spin-filtering⁵⁴ (Abelati2022PhysChemChemPhys). A nonmagnetic MA_2Z_4 state can be transformed into a magnetic one by doping of this kind at different atomic sites (M, A, or Z)⁵⁴⁻⁵⁶ (Abelati2022PhysChemChemPhys, Ding2022ApplSurfSci, Ray2021ACSomega). It can be easily perceived that by replacing metal atoms by means of substitution, doping, or alloying and by applying external strain, the magnetic behaviour of the MA_2Z_4 family of materials can be regulated to a great extent and engineered according to a targeted application. The freedom of substitution of M, A, or Z site atoms gives rise to different magnetic moments, spin channels, and conductivity suitable for the exploration of both fundamental physics and spintronic applications.

8 Valley properties

8.1 Berryology and valley-contrasting phenomena in MA_2Z_4 family

The Berry phase of the electronic wave function, along with associated physical quantities such as Berry connection and Berry curvature, can impact material properties in a plethora of spectacular and sometimes counterintuitive ways⁵⁷ (Xiao2010RevModPhys). It is responsible for a broad range of phenomena, from various types of (quantum) Hall effects and orbital magnetism to ferroelectricity and valley-contrasting physics, Fig. 3. The latter has particularly important implications for the development of advanced electronic and optoelectronic devices with enhanced performance and novel functionalities. Valley-dependent physical effects may manifest themselves in materials characterized by several local extrema (termed valleys) in the energy dispersion. In such materials, the valley degree of freedom (or valley index) can be controlled and manipulated similarly to spin degree freedom and can transfer information, encoded in its value, across the material. Valleytronics thus may offer an interesting alternative to spintronics, as the valley index is more robust with respect to smooth disorder, low-energy phonons, and mild deformations. Furthermore, spin-orbit coupling (SOC) in some multi-valley materials may promote a strong spin-valley locking, so that any impact applied to the spin degree of freedom will manipulate the valley index and vice versa paving the way for an interplay between spintronics and valleytronics studies.

8.2 Spin-valley splitting

Some representatives of the MA_2Z_4 family have been predicted to serve as an interesting platform for valleytronics and offer a convenient and versatile alternative to extensively studied transition

metal dichalcogenides (TMDC) compounds with MX_2 composition (where M stands for a transition metal and X stands for chalcogen atoms). Some MA_2Z_4 materials (e.g., $MoSi_2N_4$, WSi_2N_4 , and $MoSi_2As_4$) are characterized by two degenerate but not equivalent valleys located at the K and K' high symmetry points of the hexagonal Brillouin zone, connected by time reversal symmetry⁵⁸ (Li2020PRB). Strong spin-orbit coupling and the broken inversion symmetry, predicted in most of these materials, may result in sizable spin splitting and the emergence of non-zero Berry curvature in the conduction and valence bands, opposite for the two valleys. In some single-layer representatives of the MA_2Z_4 family, such as $CrSi_2N_4$ and $CrSi_2P_4$, the valley spin splitting is particularly pronounced and can be as large as 0.13 and 0.17 eV for $CrSi_2N_4$ and $CrSi_2P_4$, respectively⁵⁹ (Liu2021JPhysChemLett). Importantly, one of the advantages of MA_2Z_4 over TMDC MX_2 compounds in the context of valleytronics is a much larger span of available band gaps, including the technologically important mid-infrared spectrum⁶⁰ (Yuan2022PRB), which until now has only been addressed by highly biased bilayer graphene, black phosphorus, and black arsenic.

8.3 Valley-contrasting effects

MA_2Z_4 materials allow for effective steering of the valley degree of freedom using transport, optical, and magnetic means. For example, strong spin splitting in $CrSi_2N_4$ and $CrSi_2P_4$ monolayers may give rise to coexisting spin and valley Hall effects⁵⁹ (Liu2021JPhysChemLett), i.e. the emergence of valley and spin polarization perpendicularly to the applied electric field. Furthermore, valley-contrasting optical circular dichroism has been predicted to emerge in these materials. However, in contrast to TMDC MX_2 compounds, multiple-folded valleys, predicted to emerge in $MoSi_2As_4$ monolayer, enable resonant excitations of non-degenerate spin states hosted by one valley using circularly polarized light of opposite chiralities⁶¹ (Yang2021PRB). Moreover, a monolayer of VSi_2N_4 is a ferromagnetic semiconductor in which broken time reversal symmetry can lift the degeneracy between K and K' valleys⁶² (Cui2021PRB). By tuning magnetization orientation from in-plane to out-of-plane, a large valley polarization can be generated, that has been predicted to result in the anomalous valley Hall effect. Strain is another intriguing means of controlling valley polarization. Only 4% of tensile strain can cause a spontaneous polarization of VSi_2N_4 monolayer whereas biaxial strain, electric field and correlations may result in the valley counterpart of the quantum anomalous Hall effect⁶³ (Zhou2021npjCompMat).

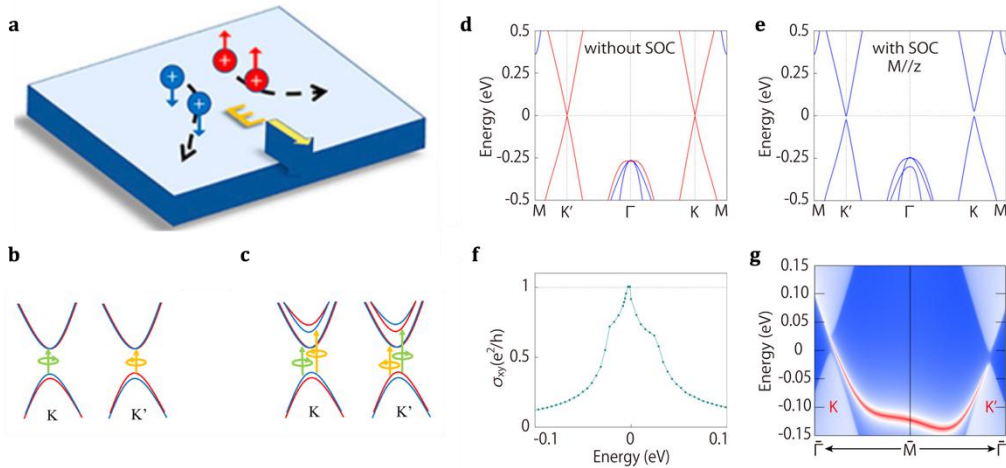


Fig. 3. Valley-contrasting properties of the MA₂Z₄ family. **a**, Diagram of the spin and valley Hall effects in hole-doped single layer CrSi₂X₄; adapted with permission from ref. ⁵⁹. **b**, Conventional valleys and **c**, multiple-folded valleys. Circles with arrows indicate the chirality of light, and arrow length denotes the photon energy. Red and blue represents up- and down-spin states, respectively; adapted with permission from ref. ⁶¹. **d – e**, Band structure of monolayer VSi₂P₄ with (e) and without (d) Spin-orbit coupling (SOC) (the red and blue colors indicate spin-up and spin-down channels, respectively). **f**, Anomalous Hall conductivity σ_{xy} versus energy for the case shown in (e). **g**, shows the corresponding edge spectrum for the quantum anomalous Hall state in (e). d – g, Adapted with permission from ref. ⁶⁴.

9 Transport Properties

Generally, a rather high intrinsic mobilities at room temperature (for instance 270 cm²/V·s for electrons 1'200 cm²/V·s for holes for MoSi₂N₄ compound¹³ (Hong2020Science)) have been predicted for semiconducting MA₂Z₄ compounds^{13,15,46,65} (Hong2020Science, Wang2021NatCommun, Zhang2022JSolidStateChem, Li2022JAP). Hole mobility is expected to be generally higher than that for electrons, which is partially because of the reduced effective mass (spin-orbit coupling being one of the reasons)^{66,67} (Qiu2022JMatChem, Mortazavi2021MatTodayEnergy). Hole mobilities exceeding 10⁵ cm²/V·s have been predicted for α_2 -WSi₂Sb₄.

Experiments indeed confirmed the semiconducting nature of MoSi₂N₄, though the mobilities observed are significantly lower than predicted¹³ (Hong2020Science). Synthesized MoSi₂N₄ films appear to be p-doped.

Interestingly, the Janus systems demonstrate^{28,68,69} (Guo2021JMaterChem, Lv2022APL, Ding2023EPL) the opposite trend than symmetric compounds: the electron mobilities are significantly higher than the hole mobilities (few thousands cm²/V·s and few hundred cm²/V·s for holes). Moreover, bilayer Janus systems can demonstrate⁶⁸ (Lv2022APL) even an order of magnitude higher mobilities – up to 58'522.3 cm²/V·s for electrons. This is due to the increase of the elastic moduli and a decrease in the deformation potential.

The performance of field effect transistors based on MoSi₂N₄ has been simulated^{70,71} (Sun2021JMaterChem, Ghobadi2022IEEE) both for the high performance and low power applications. Both n- and p-type devices have been shown to satisfy the requirements for the high-

performance applications, and the p-type transistors satisfying those for the low power ones⁷⁰ (Sun2021JMaterChem). This is because the effective mass for holes falls into the sweet range: it is high enough to guarantee a significant density of states, but low enough to secure high mobility of carriers.

Electrical contacts are extremely important for such devices. MA₂Z₄ form Schottky or Ohmic type contact with metals. The probability of a particle tunnelling through Schottky barrier in the formed structure is given by

$$P_{\text{TB}}(w_{\text{TB}}, \Phi_{\text{TB}}) = \exp\left(-2w_{\text{TB}} \frac{\sqrt{2m_e \Phi_{\text{TB}}}}{\hbar}\right) = \exp(-2w_{\text{TB}} k_{\text{TB}}), \quad (1)$$

where Φ_{TB} and w_{TB} are the height and width of the tunnelling barrier, respectively that can be estimated from the simulated charge density difference and effective electrostatic potential⁷² (Shu2023AdvElMat); $k_{\text{TB}} = \sqrt{2m_e \Phi_{\text{TB}}} / \hbar$ is the wavenumber, m_e is the free-electron mass and \hbar is the reduced Planck's constant. The tunnelling specific resistivity is calculated by using the expression of current density in a tunnel junction at intermediate voltages^{73,74} (Simmons1963JAP_p1793, Matthews2018JAP):

$$\rho_{\text{TB}}(w_{\text{TB}}, \Phi_{\text{TB}}) = \frac{4\pi^2 \hbar w_{\text{TB}}^2}{e^2} \frac{\exp(2w_{\text{TB}} k_{\text{TB}})}{w_{\text{TB}} k_{\text{TB}} - 1} \quad (2)$$

where e is the electron charge. The electronic properties of MA₂Z₄ – metal structures are summarized in Table S1 (Schottky barrier heights for electrons and holes, tunnelling barrier height and width, the tunnelling probability and resistivity, lattice mismatch and interlayer distances); the type of MA₂Z₄-metal structure as a function of (a) vertical stress (interlayer distance), (b) biaxial strain and (c) electric field are shown in Fig. S2.

Two^{75,76} (Wang2021npj2DMater, Meng2022PRA) and one⁷⁶ (Meng2022PRA)-dimensional metal contacts and well as van der Waals contacts^{77,78} (Cao2021APL, Binh2021JPhysChemLett) have been investigated. The most noticeable feature is the significantly reduce pinning of the Fermi level, because the states at both the conductance band minimum and valence band maximum are mainly localized at the central metal layer (molybdenum in the case of MoSi₂N₄). This guarantees very efficient tunability of the Schottky barrier height depending on the metal utilized for the contacts^{75,79} (Wang2021npj2DMater, Ai2023ACS_ApplelMat). Thus, Ti and Pt (as well as graphene) have been suggested among the materials suitable for good metal contacts for n- and p-type devices respectively⁷⁵ (Wang2021npj2DMater), Fig. 4. Experimentally, standard Ti/Au contacts have shown to demonstrate good Ohmic behaviour down to nitrogen temperatures¹³ (Hong2020Science).

Vertical devices have also been investigated. Thus, it has been shown that MoSi_2N_4 can be used as a barrier for magnetic tunnel junctions in combination with CrI_3 ferromagnetic contacts⁸⁰ (Liu2022PRB). Tunnelling magneto-resistance can reach $10^5\%$ due to specific arrangements between the majority/minority bands in CrI_3 and the bands in MoSi_2N_4 .

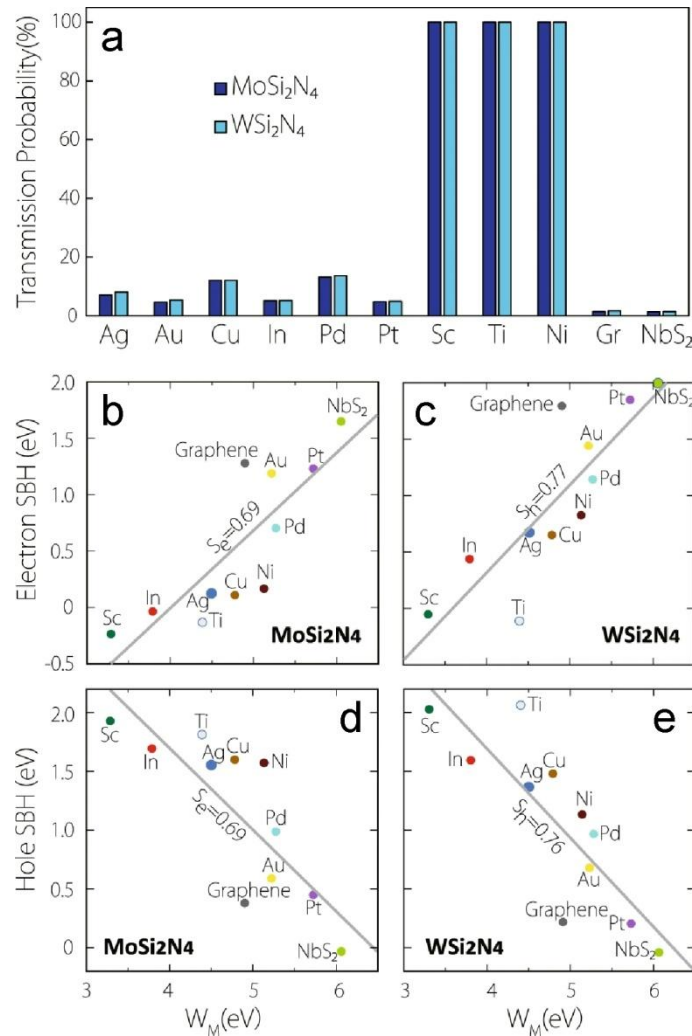


Fig. 4. Contacts to MA₂Z₄ structures. **a**, Transmission probability of various metal/ MoSi_2N_4 and metal/ WSi_2N_4 heterostructures. **b** – **c**, show the Schottky–Mott plot for the electron Schottky barrier height of MoSi_2N_4 and WSi_2N_4 , respectively. **d** – **e**, same as **b** – **c**, respectively, but for the hole Schottky barrier height. Reproduced with permission from ref. 75.

10 Topological properties

Given to a complex composition one can certainly expect that some of the members of the family indeed possess non-trivial topological properties. Indeed, it has been demonstrated^{15,81} (Wang2021NatCommun, Wang2022PRB) that a number of MA₂Z₄ compounds demonstrate inverted energy bands between $W-d_{z^2}$ and $N-p_z$ orbitals at the Γ point of the Brillouin zone. Unfortunately,

all of those have been identified as topologically trivial insulator based on the zero value of Chern number. At the same time, it has been demonstrated⁸¹ (Wang2022PRB) some MA₂Z₄ compounds can support the so called obstructed Wannier charge centres⁸² (Xu2021arXiv), when a portion of a valence electron occupies empty Wyckoff positions, with no atoms sitting at that space (materials with such properties are known as obstructed atomic insulators). In total 16 MA₂Z₄ crystals have been identified as obstructed atomic insulators.

What is most promising is that if a cleavage in a crystal passes through such obstructed Wannier charge centres – metallic edge states can be expected, which has indeed been observed⁸¹ (Wang2022PRB) for (1 $\bar{1}$) direction boundary of MoSi₂N₄ in the α_2 phase. Additionally, mid-gap corner states have been observed for both α_1 and α_2 phases of MoSi₂N₄. Such metallic edges and mid-gap states open intriguing opportunity for quantum transport.

11 Optical properties

The diverse family of 2D MA₂Z₄ includes semiconductors with band gaps ranging from infrared to ultraviolet ranges. Overall, the band gap of the MA₂Z₄ monolayer can vary between 0.3–2.57 eV, making it drastically different from conventional transition metal dichalcogenide (TMD) crystals whose band gap range falls into the visible/near-IR range³⁴ (Mortazavi2021NanoEnergy). The substitution of any of the three elements (M/A/Z) with an element from a similar category or alloying can alter the band structure analogous to the TMDs⁸³ (Gong2014NanoLetters). For example, the substitution of N-atoms by As- or P-atoms affects the band gap and changes the nature of the nearest interband transition. The onset of optical absorption of MoSi₂N₄ is predicted in the visible region (~2.31 eV), whereas that of for MoSi₂As₄ falls in the near-infrared range (0.71 eV)⁸⁴ (Sun2022npj2DMater). Furthermore, band structure calculations show that monolayers MA₂N₄ (e.g., MoSi₂N₄) generally exhibit an indirect band gap, whereas MA₂As₄ materials (e.g., MoSi₂As₄ or MoSi₂P₄) are expected to be direct band gap semiconductors⁸⁴ (Sun2022npj2DMater). Generally, heavier M-atoms (e.g., W compared to Mo) can induce a pronounced red shift in the band gap compared to the lighter ones^{34,58,84-86} (Mortazavi2021NanoEnergy, Sun2022npj2DMater, Yang2022PRB, Li2022Nanomaterials, Li2020PRB). Finally, the band structure can be altered, and light absorption capacity can be increased by applying strain to the layers and employing surface functionalization^{87,88} (Zhang2023RSCadv, Liu2023PhysChemChemPhys). The described tunability of the band structure in the 2D MA₂Z₄ family makes it promising for polarization-sensitive broadband optoelectronic devices.

Excitons dominate the optical properties in 2D MA₂Z₄ as they have high binding energy, similarly to TMD. These materials exhibit excitonic (A & B) absorption features related to spin-orbit

coupling-induced band splitting similar to that observed in 2D TMDs and display analogous selection rules for polarized light corresponding to different valleys^{13,84,89} (Hong2020Science, Sun2022npj2DMaterAppl, Selig2019PhysRevRes). Higher energy direct interband optical transitions (exciton 'C') with prominent absorption feature is also predicted in layered MA₂Z₄ (Fig. 5)^{84,90} (Sun2022npj2DMater, Aleithan2016PRB). Similarly to TMDCs, excitons in these materials exhibit high exciton binding energy up to a few hundred meV, which makes them stable against thermal dissociation at room temperature and suitable for excitonic device applications^{13,84,89,91,92} (Hong2020Science, Sun2022npj2DMater, Selig2019PhysRevRes, Ai2021PhysChemChemPhys, Wozniak2023Small). However, the presence of the outer SiX layers affects exciton binding energies making them smaller than those generally found in TMDC compounds⁸⁴. The lifetime of excitons τ_x in 2D semiconductors is proportional to M_x – the effective mass of the exciton, and inversely proportional to the square of E_x – the energy of exciton at zero momentum: $\tau_x \propto M_x / E_x^2$ ⁹³⁻⁹⁵ (Palummo2015NanoLett, Chen2018NanoLett, Chen2019PRB). As shown in ref.⁸⁴ (Sun2022npj2DMater), τ_x in MoSi₂N₄ are comparable to that found in most common TMDs (e.g., MoS₂, MoSe₂, and WSe₂) and is of the order of 1-7 ns at liquid helium temperatures and around 1 ns at room temperature. In contrast, the values for MoSi₂P₄ and MoSi₂As₄ are approximately two orders of magnitude greater. For example, record high values of τ_x reaching 370 and 28 ns were predicted in MoSi₂As₄ at 4 K and 300 K respectively⁸⁴ (Sun2022npj2DMater). This difference was associated with the low exciton energy and the elevated effective mass of the excitons. Besides, the absence of nearby valleys around the band extrema can reduce non-radiative pathways in MoSi₂Z₄ nano-sheets, favouring a higher rate of radiative recombination of photo-generated electrons and holes with a higher quantum yield of luminescence⁸⁴ (Sun2022npj2DMater). Last, we envision that heterostructures composed of various MA₂Z₄ monolayers with aligned or twisted crystallographic axes⁹⁶ (Zhong2023PRB) may offer a whole new class of interaction-driven phenomena and give rise to rich phase diagrams⁹⁷ (Mak2022NatNanotech).

We also note that, recently, new exciton states have been discovered in 2D semiconductors termed quadrupolar and every-other-layer excitons⁹⁸ (Du2024NatureRevPhys). These excitons are characterized by an electrically-tunable dipole moment and feature a many-body phase diagram. Considering that the strong exciton-phonon coupling⁹⁹ (Huang2022AdvOptMat) and exciton self-trapping effect¹⁰⁰ (Huang2023AdvOptMat) were reported for MoSi₂N₄, we envision that interesting forms of these new tunable exciton states can be also observed in single- few-layer MA₂Z₄ sheets.

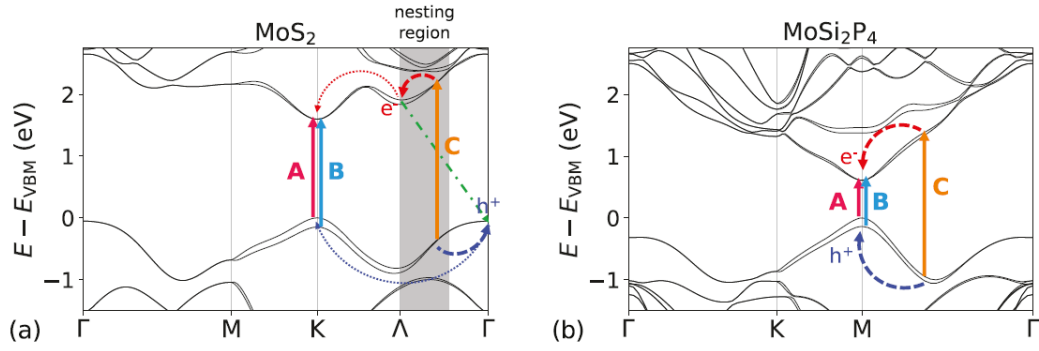


Fig. 5 Different excitons in (a) MoS₂ and (b) MoSi₂P₄ materials and the typical relaxation processes. Adapted with permission from ref. 84.

12 Heterostructures

The alignment of the energy bands in MA₂Z₄-semiconductor heterostructures can be of normal (I), staggered (II) and broken gap (III) type (Fig. 6a). Liu et al simulated band structures of six perovskites A₃BX₉ (A = Cs; B = In, Sb, Bi; and X = Cl, Br, I) and six MA₂N₄ (M = Cr, Mo, Ti; A = Si; and Z = N, P) materials and showed that A₃B₂X₉/MA₂Z₄ heterostructures can exhibit all three types of band alignment (I, II and III)¹⁰¹ (Liu2022JApplPhys). Type II alignment is the preferred band alignment, for it allows for an effective electrons and holes separation, avoiding their recombination and thus extending the lifetimes of these charge carriers. External vertical or biaxial strain, or electric field cause charge redistribution within and between the layers, which in turn changes the bands distribution of the overall structure. Thus, these external forces can tune the band alignment type (I, II or III), the band gap value, and the band gap type (direct, indirect)¹⁰²⁻¹¹¹ (Fang2022PhysicaE, Nguyen2022PRB, Ng2022APL, Xu2023JPhysChemC, Cai2021JMatChemC, Wu2021APL, Pei2023PhysicE, Nguyen2021JPhysChemLett, Wang2021Nanomaterials, Zhang2023JAlloysComp). The applied strain is typically varied in the range of ±10%, and the applied electric field within the range ±0.5 V/Å. The bandgap typically decreases under applied strain or electric field, ultimately reaching zero. As an example, MoSi₂N₄/MoS₂ structure changing its electronic properties under applied biaxial strain and electric field is shown in Fig. 6b-f¹⁰⁵ (Xu2023JPhysChemC) (Fig. 6b-f).

Various heterostructures created by combining MA₂Z₄ layer combined with semiconductors, metals, dielectrics, and laterally stitched structures were recently overviewed by Tho et al.¹¹² (Tho2023_ApplPhysRev). The electronic properties of MA₂Z₄-based vdWHs are summarized in TableS2; the band alignment and bandgap type (direct, indirect) as a function of (a) vertical stress (interlayer distance), (b) biaxial strain and (c) electric field are shown in Fig. S3.

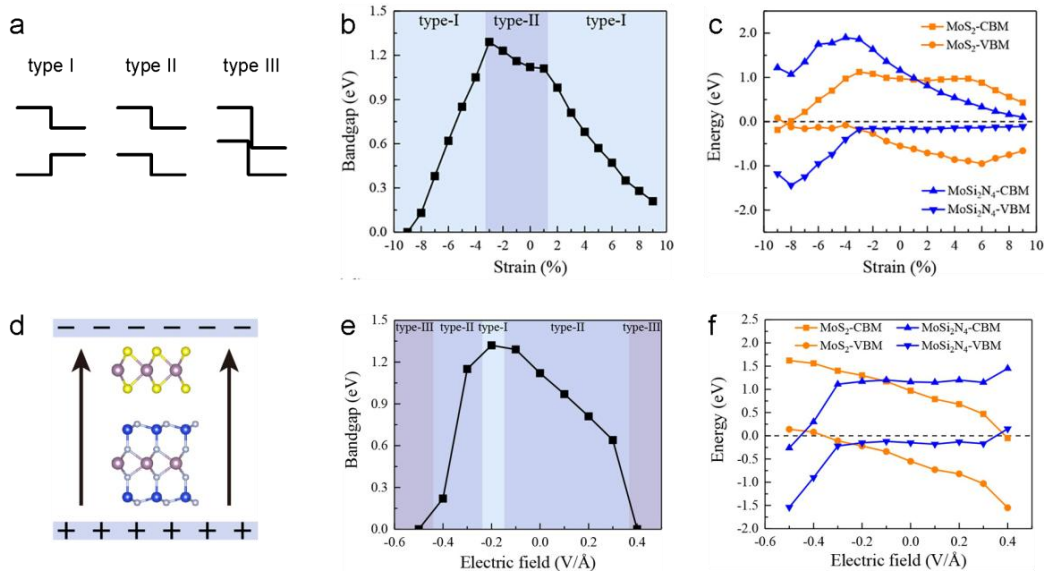


Fig. 6 Band alignment and energy gaps in $\text{MoSi}_2\text{N}_4/\text{MoS}_2$ van der Waals heterostructure. **a**, Three types of band alignment. **b – c**, Band gap and alignment type under biaxial strain. **d – f**, Band gap and alignment type under external electric field, (**d**) shows the direction of electric field. The Fermi level in (**c**) and (**f**) is set to zero. **b – f** adapted with permission from ref. 105.

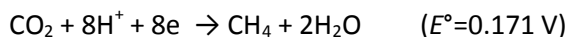
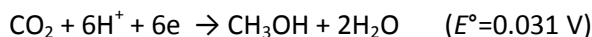
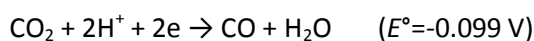
An integrated system from such a vast library of MA_2Z_4 materials in combination with other 2D materials (such as graphene or TMDs) in a van der Waals heterostructure (vdWH) arrangement can exhibit optical absorption beneficial for realizing photodetectors with extended operational bandwidth. Various 2D materials with varying optical properties and conductivity can be employed in high-quality, ultraclean vertical all-2D vdWH devices of sizeable interfacial areas for broadband operation^{78,113,114} (Bafekry2021NewJChem, Binh2021JPhysChemLett, Cai2022Crystals). In particular, a type-II band alignment between two adjacent semiconductors is desired for rapid separation of charge carriers before recombination across a heterointerface for photovoltaic applications. TMDs/ MA_2Z_4 heterojunctions usually exhibit a type-I alignment (the alignment types are shown in Fig. 6a). However, applying an electric field or external strain can shift the alignment to staggered ones (type-II)¹⁰⁶ (Cai2021JMaterChem). Boron phosphide/ MoSi_2P_4 or boron phosphide/ MoGe_2N_4 are some of the direct band gap vdWHs that inherently form type-II band alignment^{109,115} (Guo2022JPhysChem, Nguyen2021JPhysChemLett). Likewise, interlayer coupling and faster charge separation across a blue-P/ MoSi_2N_4 type-II heterojunction are found to be beneficial for photocatalytic and photovoltaic applications¹¹⁴ (Cai2022Crystals). $\text{MoSi}_2\text{N}_4/\text{Cs}_3\text{Bi}_2\text{I}_9$ heterostructure is reported to exhibit broadband absorption, which is absent in the individual materials¹⁰¹ (Liu2022JAP). Hence, this class of materials is promising for integrated multicolor photonic devices such as photodetectors, photovoltaic cells, and optical modulators.

13 Catalytic properties

Many 2D materials have already proven themselves as excellent catalysts¹¹⁶⁻¹¹⁹ (Deng2016NatNanotech, Deng2017NatCommun, Voiry2016AdvMat, Zhang2020ApplSurfSci). Due to the presence of transition metals¹²⁰⁻¹²⁴ (Twilton2017NatRevChem, Peng2019JMatChemA, Yu2020AdvFunctMat, Zhang2021JMatChemA, Wang2022ApplSurfSci), MA₂Z₄ (M=Mo, W) materials can also be added to the line of the promising 2D candidates to serve as catalysts in water splitting, CO₂ reduction and other photochemical reaction due to their broadly tunable photochemical properties. In a photochemical reaction, a photon of light, absorbed by the catalyst, generates an electron-hole pair, these charges then migrate to the catalyst's surface where they participate in the chemical reaction. A suitable photocatalyst thus should: exhibit a large electrochemical active surface area (ECSA) – this requirement is fulfilled for all 2D materials; be stable at room temperature; its energy gap should be smaller than the energy of visible light photon (3.26 – 1.77 eV corresponding to 380 – 700 nm) in order to be able to absorb the light; its absorption coefficient in the visible light range should be comparable or exceeding 10⁵ cm⁻¹. In addition, the photocatalyst should have a built-in option for separating the created electrons and holes to avoid their recombination, and exhibit high charge carriers mobility. As suitable catalysts, semiconductors with direct band gap are preferred since they allow direct electron transition from valence to conduction band, without a need of phonon creation to fulfil the energy and momentum conservation laws. The band edges of the catalyst should straddle the potentials of the reactions: its valence band edge (VBE) or valence band maximum (VBM) should be lower than the potential of an oxidation reaction, and its conduction band edge (CBE) or conduction band minimum (CBM) should be larger than the potential of a redox reaction, as illustrated in Fig. 7a. Reaction potential depends on pH as defined by the Nernst equation: $E^{\circ}(\text{pH}) = E^{\circ}(\text{pH}=0) + \text{pH} \cdot 0.059 \text{ eV}$, (at 25° C). The band edges of a semiconductor can be evaluated either directly from its energy bands distribution, or from its bandgap E_g alone by using the following equations¹²⁵ (Liu2011APL): $E_{\text{VBE}} = x - 4.5\text{eV} + 0.5E_g$, and $E_{\text{CBE}} = E_{\text{VBE}} - E_g$, where x is the geometric average value of the electronegativity of the constituent atoms ($x = 5.195$ for MoSi₂N₄¹²⁶ (Bartolotti1980JACS)), and 4.5 eV is the energy of free electrons on the hydrogen scale.

The water splitting reaction $\text{H}_2\text{O} \rightarrow \text{H}_2 + 1/2\text{O}_2$ consists of two half-reactions¹²⁷ (Nishioka2023NatRevMethods): hydrogen evolution reaction (HER) $2\text{H}^+ + 2\text{e}^- \rightarrow \text{H}_2$ and oxygen evolution reaction (OER) $\text{H}_2\text{O} + 2\text{h}^+ \rightarrow 1/2\text{O}_2 + 2\text{H}^+$. Thus, the catalyst's VBE should be lower than the potential of the OER ($E(\text{H}_2\text{O}/\text{O}_2) = -5.67 \text{ eV} + \text{pH} \cdot 0.059 \text{ eV}$), its CBE should be higher than the

potential of HER ($E(\text{H}^+/\text{H}_2) = -4.44 \text{ eV} + \text{pH} \cdot 0.059 \text{ eV}$), with the minimal energy gap of 1.23 eV. Photocatalytic CO_2 reduction reaction can be realized by one of the following reactions:



The potentials E° shown here (vs standard hydrogen electrode (SHE) at $\text{pH}=0$) were calculated using the free energy¹²⁸ (Latimer_book). The positions of the potentials for water splitting and CO_2 reduction reactions, together with the band edges of a hypothetically suitable catalyst are shown in Figure 7a.

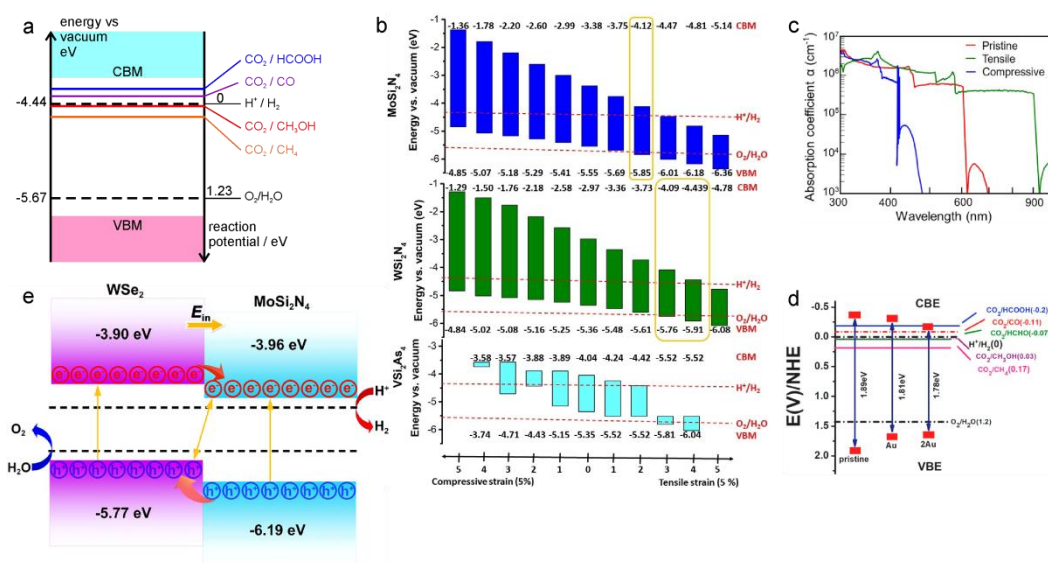


Fig. 7 Photocatalytic properties of MA_2Z_4 materials. **a**, Potentials of the water splitting and CO_2 reduction reactions, shown together with the conduction and valence band edges (CBE and VBE, respectively) of a hypothetically suitable catalyst. **b**, Calculated band edges of WSi_2N_4 , MoSi_2N_4 and VSi_2As_4 at applied biaxial strain shown relatively to the vacuum level; adapted with permission from ref. 48. **c**, Optical absorption coefficients of pristine and strained ($\varepsilon = +6\%$ and -6%) MoSi_2N_4 monolayers as a function of wavelength; adapted with permission from ref. 129. **d**, Band alignments of intrinsic MoSi_2N_4 and $\text{MoSi}_2\text{N}_4\text{-nAu}$ ($n=1, 2$) for photocatalytic water splitting and carbon dioxide reduction. The band edges are given with respect to the NHE (normal hydrogen electrode) potential (V); adapted with permission from ref. 130. **e**, Schematic diagram of the photocatalytic reaction for the $\text{WSe}_2/\text{MoSi}_2\text{N}_4$ type-II heterostructure. E_{in} denotes the direction of the built-in electric field; adapted with permission from ref. 131.

The bandstructure of MA_2Z_4 materials suggest that some of these materials can be promising catalysts for photocatalytic water splitting or CO_2 reduction reactions. Moreover, biaxial strain can boost the photocatalytic properties by shifting the band edges^{29,48} (Yu2021ApplMatInterfaces, Chen2021ChemistryAEuropeanJ) and increasing the absorption coefficient^{129,132} (Jian2021JPhysChem, Xuefeng2022JPhysD). Chen et al investigated 54 MA_2Z_4 materials and found that only three materials have bandgaps larger than $E_g = 1.23 \text{ eV}$ and thus can be suitable catalyst for water splitting reaction: MoSi_2N_4 ($E_g = 2.13 \text{ eV}$), WSi_2N_4 ($E_g = 2.38 \text{ eV}$) and VSi_2As_4 ($E_g = 1.31 \text{ eV}$).

However, the band edges of these structures straddle the reaction potentials only when biaxial tensile strain is applied: $\varepsilon = 2\%$ for MoSi_2N_4 and $\varepsilon = 3\text{--}4\%$ for WSi_2N_4 ⁴⁸ (Chen2021ChemistryAEuropeanJ), Fig. 7b. The measured absorption coefficient of pristine MoS_2N_4 is close to zero at wavelengths exceeding 650 nm¹³ (Hong2020Science), but can be increased by shifting the spectrum towards longer wavelengths when biaxial tensile strain of $\varepsilon = 6\%$ is applied¹²⁹ (Jian2021JPhysChem), Fig. 7c.

In single-atom catalysts (SACs), transition metals (TM) are the most popular choice for SACs structures in MA_2Z_4 family, for their partially filled d-orbitals that allow for both donating and accepting electrons¹³³⁻¹³⁵ (Sun2022PhysChemCh, Lu2022ApplSurfSci, Xun2023ApplEnMat). DFT study of 15 single metal atom-doped 2D MA_2Z_4 (TM1/ MA_2Z_4) showed that $\text{Cr}_1/\text{HfSi}_2\text{N}_4$ is the ideal catalyst candidate for the NO reduction reaction (NORR) (Sun2022PhysChemCh). Using first-principle calculations, 5 (Sc, Ti, Fe, Co, Ni) out of 10 TMs on MoSi_2N_4 were identified as suitable SACs for CO_2 reduction¹³⁵ (Xun2023ApplEnMat). Alkali-metal (Li, Na, or K) adsorbed on MoSi_2N_4 greatly increase the absorption coefficient α in the visible light range (380 – 780nm) when compared to pristine MoSi_2N_4 : $\alpha = 0.34 - 0.02$ (pristine), $0.57 - 0.92$ (Li), $1.09 - 1.34$ (Na), and $0.89 - 1.14$ (K) $\times 10^5 \text{ cm}^{-1}$ (Fig. 7d), respectively¹³⁶ (Sun2022CommunTheorPhys). Similarly, adding one or two Au atoms to MoSi_2N_4 increases α (Fig. 7e), however adding more than 3 Au atoms decreases the band gap, eventually turning it to zero when 9 Au atoms are added¹³⁰ (Xu2022JPhysChemSolids).

In pristine MoSi_2N_2 , both VBM and CBM are mainly contributed by Mo atoms¹³⁰ (Xu2022JPhysChemSolids), thus creating a high probability for recombination of the photo-generated electrons and holes. This issue can be resolved by placing MoSi_2N_2 into a van der Waals structure, where the redistributed charge creates a built-in electric field that can effectively separate the photo-generated charges. In van der Waals structures, the atoms that contribute to VBM and CBM can be from different, spatially separated layers, which leads to a better separation between photo-generated charges. For example, in AB-stacking bilayer MoSi_2N_4 , the CBM and VBM are dominated by the states of the Mo atoms in the lower and upper layer, respectively¹³⁷ (Zhao2021JPhysChemLett). The built-in electric field transports the charges to the catalyst surface, and two parts of a reaction (oxidation and reduction) can run on the two sides of the catalyst (Fig. 6f). Besides bilayer MoSi_2N_4 and $(\text{MoSi}_2\text{N}_4)_{5-n}/(\text{MoSiGeN}_4)_n$ ($n=0,\dots,5$)¹³⁸ (Mwankemwa2022ResPhys), the following MoS_2N_4 -based vdWH were proposed as efficient photocatalysts: $\text{C}_2\text{N}/\text{MoS}_2\text{N}_4$ for HER reaction¹³⁹ (Zeng2021PhysChemChemPhys), $\text{MoS}_2\text{N}_4/\text{CrS}_2$ ¹⁴⁰ (Li2022PhysicaE), $\text{InSe}/\text{MoS}_2\text{N}_4$ ¹⁴¹ (He2022PhysChemChemPhys), $\text{Mo}_5\text{N}_4/\text{BlueP}$ ¹³² (Xuefeng2022JPhysDAppPhys) and $\text{WS}_2/\text{MoS}_2\text{N}_4$ ¹³¹ (Liu2023ApplSurfSci) for photocatalytic water splitting. The catalytic properties of MA_2Z_4 materials are summarized in Table S3.

In Janus structures MSiGeN_4 ($M = \text{Mo}$ and W)²⁸ (Guo2021JMaterChemC), breaking the vertical symmetry of the structure creates a significant built-in electric field which can enhance the charge separation. Janus structures MoSiGeN_4 and WSiGeN_4 were found as potential catalysts for photocatalytic water splitting²⁹ (Yu2021ApplMatInterf). Zhang et al screened 104 Janus- MA_2Z_4 structures and identified 13 thermally and environmentally stable structures; from which HfSiGeP_4 , HMoSiGeP_4 , T-ScSiGeN_4 , and T-ZrSiGeN_4 are suitable photocatalysts for CO_2 reduction reactions¹⁴² (Zhang2022FrontPhys). The photocatalytic properties of MA_2Z_4 materials are summarized in Table S1. In addition, DFT studies by Chen et al identified 42 dynamically stable MA_2Z_4 ($M = \text{Ti, Zr, Hf, V, Nb, Ta, Cr, Mo, W}$; $A = \text{Si or Ge}$; $Z = \text{N, P, or As}$) monolayers, where four of them, VGe_2As_4 , CrGe_2As_4 , VSi_2As_4 , and NbSi_2As_4 , are predicted to exhibit promising oxygen reduction reaction (ORR) electrocatalytic activity⁴⁸ (Chen2021ChemA).

Relatively small negative adsorption energies of environmental gas molecules (H_2 , N_2 , NO , CO , O_2 , CO_2 , NO_2 , SO_2 , H_2O , H_2S , NH_3 , and CH_4) on MoSi_2N_4 surface (physisorption) suggest the possibility of using MoSi_2N_4 monolayers as gas sensors^{143,144} (Xiao2022ACS_Omega, Bafekry2021ApplSurfSci). The abovementioned optical properties of MoSi_2N_4 and their heterostructures – appropriate band gap, high absorption coefficient, high carriers' mobility – make these materials promising candidates for solar cells. The predicted photoelectric conversion efficiency (PCE) for the $\text{BP/MoSi}_2\text{P}_4$ heterostructure of 22.2% is the largest PCE among 2D heterostructures¹¹⁵ (Guo2022JPhysChemC).

14 Conclusions

The new class of septuple layer two-dimensional material will offer new opportunities and functionalities when searching for new quantum phenomena in transport and optical properties of such materials, as well as investigating new van der Waals heterostructures. Crystals with a range of properties (metallic, semiconducting, ferromagnetic, superconducting, etc) have been predicted to be the members of the class. What is unique about such materials, is that the seven atomic layers thick unit cell offers a lot of variation both in terms of chemical composition and the crystal phase formation, thus allowing for a lot of tunability as well as observation of multiple phase transitions. We envisage that the multitude of the phases available can result in structural and electronic phase transitions observed under ambient conditions, which might be important for novel electronic (like neuromorphic computing, for instance). Thus, in optical applications, MA_2Z_4 can act as a polarization-sensitive element with broadband responsivity spanning across visible to mid-IR frequency domains while some semiconducting MA_2Z_4 materials with magnetic order can offer novel spintronic applications. Furthermore, the relatively large thickness of the crystals can allow the generation of

transversal electric field, which can non-trivially alter the electronic, optical, mechanical and other properties. This is especially important for photo-catalysis, since it allows for efficient electron-hole separation, which is not observed in other 2D materials. The first member of the group - MoSi₂N₄ – was recently synthesised using seemingly simple technique. Still, despite the plethora of intriguing predictions – the experimental growth of other members of the family is lagging behind. At the same time, there is no indication that there are any fundamental limitations which can impede the progress in this area, so we can expect more similar crystals to appear in the near future. As this family of materials has a very rich compositional and structural variety, the use of machine learning for the design and synthesis of such crystals might be beneficial, as indeed has already been implemented in the other areas of material science^{145,146} (Merchant2023Nature, Hippalgaonkar2023NatRevMat), including 2D materials¹⁴⁷⁻¹⁴⁹ (Kazeev2023npjCompMat, Huang2023npj2DMatAppl, Sun2023ACSAppMatInterf). We hope that this review will instigate further experimental activity in this area.

References

- 1 Novoselov, K. S. *et al.* Electric field effect in atomically thin carbon films. *Science* **306**, 666–669, doi:10.1126/science.1102896 (2004).
- 2 Novoselov, K. S. *et al.* Two-dimensional atomic crystals. *PNAS* **102**, 10451–10453, doi:10.1073/pnas.0502848102 (2005).
- 3 Nicolosi, V., Chhowalla, M., Kanatzidis, M. G., Strano, M. S. & Coleman, J. N. Liquid exfoliation of layered materials. *Science* **340**, 1226419, doi:10.1126/science.1226419 (2013).
- 4 Bhimanapati, G. R. *et al.* Recent advances in two-dimensional materials beyond graphene. *ACS Nano* **9**, 11509–11539, doi:10.1021/acsnano.5b05556 (2015).
- 5 Cai, Z., Liu, B., Zou, X. & Cheng, H.-M. Chemical vapor deposition growth and applications of two-dimensional materials and their heterostructures. *Chem. Rev.* **118**, 6091–6133, doi:10.1021/acs.chemrev.7b00536 (2018).
- 6 Naguib, M. *et al.* Two-dimensional nanocrystals produced by exfoliation of Ti₃AlC₂. *Adv. Mater.* **23**, 4248–4253, doi:10.1002/adma.201102306 (2011).
- 7 Naguib, M. *et al.* Two-dimensional transition metal carbides. *ACS Nano* **6**, 1322–1331, doi:10.1021/nn204153h (2012).
- 8 Naguib, M., Mochalin, V. N., Barsoum, M. W. & Gogotsi, Y. 25th Anniversary article: MXenes: A new family of two-dimensional materials. *Adv. Mater.* **26**, 992–1005, doi:10.1002/adma.201304138 (2014).
- 9 Guo, Z., Zhou, J. & Sun, Z. New two-dimensional transition metal borides for Li ion batteries and electrocatalysis. *Journal of Materials Chemistry A* **5**, 23530–23535, doi:10.1039/c7ta08665b (2017).
- 10 Zhang, H., Xiang, H., Dai, F.-z., Zhang, Z. & Zhou, Y. First demonstration of possible two-dimensional MBene CrB derived from MAB phase Cr₂AlB₂. *J. Mater. Sci. Technol.* **34**, 2022–2026, doi:10.1016/j.jmst.2018.02.024 (2018).
- 11 Alameda, L. T., Moradifar, P., Metzger, Z. P., Alem, N. & Schaak, R. E. Topochemical deintercalation of Al from MoAlB: Stepwise etching pathway, layered Intergrowth structures, and two-dimensional MBene. *Journal of the American Chemical Society* **140**, 8833–8840, doi:10.1021/jacs.8b04705 (2018).

- 12 Zhang, B., Zhou, J. & Sun, Z. MBenes: progress, challenges and future. *Journal of Materials Chemistry A* **10**, 15865–15880, doi:10.1039/d2ta03482d (2022).
- 13 Hong, Y.-L. *et al.* Chemical vapor deposition of layered two-dimensional MoSi₂N₄ materials. *Science* **369**, 670–674, doi:10.1126/science.abb7023 (2020).
- 14 Novoselov, K. S. Discovery of 2D van der Waals layered MoSi₂N₄ family. *National Science Review* **7**, 1842–1844, doi:10.1093/nsr/nwaa190 (2020).
- 15 Wang, L. *et al.* Intercalated architecture of MA₂Z₄ family layered van der Waals materials with emerging topological, magnetic and superconducting properties. *Nat. Commun.* **12**, 2361, doi:10.1038/s41467-021-22324-8 (2021).
- 16 Lee, D. S. *et al.* Crystal structure, properties and nanostructuring of a new layered chalcogenide semiconductor, Bi₂MnTe₄. *CrystEngComm* **15**, 5532–5538, doi:10.1039/c3ce40643a (2013).
- 17 Gong, Y. *et al.* Experimental realization of an intrinsic magnetic topological insulator. *Chinese Physics Letters* **36**, 076801, doi:10.1088/0256-307x/36/7/076801 (2019).
- 18 Peng, Y. & Xu, Y. Proximity-induced Majorana hinge modes in antiferromagnetic topological insulators. *Phys. Rev. B* **99**, 195431, doi:10.1103/PhysRevB.99.195431 (2019).
- 19 Li, J. *et al.* Intrinsic magnetic topological insulators in van der Waals layered MnBi₂Te₄-family materials. *Sci. Adv.* **5**, eaaw5685, doi:10.1126/sciadv.aaw5685 (2019).
- 20 Zhang, D. *et al.* Topological axion states in the magnetic insulator MnBi₂Te₄ with the quantized magnetoelectric effect. *Phys. Rev. Lett.* **122**, 206401, doi:10.1103/PhysRevLett.122.206401 (2019).
- 21 Otrokov, M. M. *et al.* Unique thickness-dependent properties of the van der Waals interlayer antiferromagnet MnBi₂Te₄ films. *Phys. Rev. Lett.* **122**, 107202, doi:10.1103/PhysRevLett.122.107202 (2019).
- 22 Deng, Y. *et al.* Quantum anomalous Hall effect in intrinsic magnetic topological insulator MnBi₂/Te₄. *Science* **367**, 895–900, doi:10.1126/science.aax8156 (2020).
- 23 Gao, A. *et al.* Layer Hall effect in a 2D topological axion antiferromagnet. *Nature* **595**, 521–525, doi:10.1038/s41586-021-03679-w (2021).
- 24 Otrokov, M. M. *et al.* Prediction and observation of an antiferromagnetic topological insulator. *Nature* **576**, 416–422, doi:10.1038/s41586-019-1840-9 (2019).
- 25 He, K. MnBi₂Te₄-family intrinsic magnetic topological materials. *npj Quantum Materials* **5**, 90, doi:10.1038/s41535-020-00291-5 (2020).
- 26 Liu, Z. *et al.* Two-dimensional superconducting MoSi₂N₄(MoN)_{4n} homologous compounds. *National Science Review* **10**, nwac273, doi:10.1093/nsr/nwac273 (2023).
- 27 Zhang, L. *et al.* Recent advances in emerging Janus two-dimensional materials: from fundamental physics to device applications. *Journal of Materials Chemistry A* **8**, 8813–8830, doi:10.1039/d0ta01999b (2020).
- 28 Guo, S.-D., Mu, W.-Q., Zhu, Y.-T., Han, R.-Y. & Ren, W.-C. Predicted septuple-atomic-layer Janus MSiGeN₄ (M = Mo and W) monolayers with Rashba spin splitting and high electron carrier mobilities. *Journal of Materials Chemistry C* **9**, 2464–2473, doi:10.1039/d0tc05649a (2021).
- 29 Yu, Y., Zhou, J., Guo, Z. & Sun, Z. Novel two-dimensional Janus MoSiGeN₄ and WSiGeN₄ as highly efficient photocatalysts for spontaneous overall water splitting. *ACS Appl. Mater. Interfaces* **13**, 28090–28097, doi:10.1021/acscami.1c04138 (2021).
- 30 Guo, S.-D., Zhu, Y.-T., Mu, W.-Q. & Chen, X.-Q. A piezoelectric quantum spin Hall insulator with Rashba spin splitting in Janus monolayer SrAlGaSe₄. *Journal of Materials Chemistry C* **9**, 7465–7473, doi:10.1039/d1tc01165k (2021).
- 31 Li, Q., Zhou, W., Wan, X. & Zhou, J. Strain effects on monolayer MoSi₂N₄: Ideal strength and failure mechanism. *Physica E: Low-dimensional Systems and Nanostructures* **131**, 114753, doi:10.1016/j.physe.2021.114753 (2021).

- 32 Guo, S.-D., Zhu, Y.-T., Mu, W.-Q., Wang, L. & Chen, X.-Q. Structure effect on intrinsic piezoelectricity in septuple-atomic-layer MSi_2N_4 (M=Mo and W). *Computational Materials Science* **188**, 110223, doi:10.1016/j.commatsci.2020.110223 (2021).
- 33 Bafekry, A. *et al.* MoSi_2N_4 single-layer: a novel two-dimensional material with outstanding mechanical, thermal, electronic and optical properties. *Journal of Physics D: Applied Physics* **54**, 155303, doi:10.1088/1361-6463/abdb6b (2021).
- 34 Mortazavi, B. *et al.* Exceptional piezoelectricity, high thermal conductivity and stiffness and promising photocatalysis in two-dimensional MoSi_2N_4 family confirmed by first-principles. *Nano Energy* **82**, 105716, doi:10.1016/j.nanoen.2020.105716 (2021).
- 35 Blonsky, M. N., Zhuang, H. L., Singh, A. K. & Hennig, R. G. Ab initio prediction of piezoelectricity in two-dimensional materials. *ACS Nano* **9**, 9885–9891, doi:10.1021/acs.nano.5b03394 (2015).
- 36 Duerloo, K.-A. N., Ong, M. T. & Reed, E. J. Intrinsic piezoelectricity in two-dimensional materials. *The Journal of Physical Chemistry Letters* **3**, 2871–2876, doi:10.1021/jz3012436 (2012).
- 37 Geim, A. K. & Grigorieva, I. V. Van der Waals heterostructures. *Nature* **499**, 419–425, doi:10.1038/nature12385 (2013).
- 38 Novoselov, K. S., Mishchenko, A., Carvalho, A. & Neto, A. H. C. 2D materials and van der Waals heterostructures. *Science* **353**, aac9439, doi:10.1126/science.aac9439 (2016).
- 39 Woods, C. R. *et al.* Charge-polarized interfacial superlattices in marginally twisted hexagonal boron nitride. *Nat. Commun.* **12**, 347, doi:10.1038/s41467-020-20667-2 (2021).
- 40 Vizner Stern, M. *et al.* Interfacial ferroelectricity by van der Waals sliding. *Science* **372**, 1462–1466, 2021).
- 41 Weston, A. *et al.* Interfacial ferroelectricity in marginally twisted 2D semiconductors. *Nature Nanotechnology* **17**, 390–395, doi:10.1038/s41565-022-01072-w (2022).
- 42 Zhong, T., Ren, Y., Zhang, Z., Gao, J. & Wu, M. Sliding ferroelectricity in two-dimensional MoA_2N_4 (A = Si or Ge) bilayers: high polarizations and Moiré potentials. *Journal of Materials Chemistry A* **9**, 19659–19663, doi:10.1039/d1ta02645c (2021).
- 43 Yang, Q., Wu, M. & Li, J. Origin of two-dimensional vertical ferroelectricity in WTe_2 bilayer and multilayer. *The Journal of Physical Chemistry Letters* **9**, 7160–7164, doi:10.1021/acs.jpcclett.8b03654 (2018).
- 44 Yin, Y., Yi, M. & Guo, W. High and anomalous thermal conductivity in monolayer MSi_2Z_4 semiconductors. *ACS Appl. Mater. Interfaces* **13**, 45907–45915, doi:10.1021/acsami.1c14205 (2021).
- 45 Yu, J., Zhou, J., Wan, X. & Li, Q. High intrinsic lattice thermal conductivity in monolayer MoSi_2N_4 . *New J. Phys.* **23**, 033005, doi:10.1088/1367-2630/abe8f7 (2021).
- 46 Zhang, C. *et al.* Thermoelectric properties of monolayer MoSi_2N_4 and MoGe_2N_4 with large Seebeck coefficient and high carrier mobility: A first principles study. *Journal of Solid State Chemistry* **315**, 123447, doi:10.1016/j.jssc.2022.123447 (2022).
- 47 Zhao, Z., Duan, X., Fang, X., Wang, X. & Mi, W. Prediction of electronic structure and magnetic anisotropy of two-dimensional MSi_2N_4 (M = 3d transition-metal) monolayers. *Appl. Surf. Sci.* **611**, 155693, doi:10.1016/j.apsusc.2022.155693 (2023).
- 48 Chen, J. & Tang, Q. The versatile electronic, magnetic and photo-electro catalytic activity of a new 2D MA_2Z_4 family**. *Chemistry – A European Journal* **27**, 9925–9933, doi:10.1002/chem.202100851 (2021).
- 49 Li, Y. & Liu, Y. Stable ferromagnetism and high Curie temperature in VGe_2N_4 . *New J. Phys.* **24**, 083008, doi:10.1088/1367-2630/ac8239 (2022).
- 50 Feng, Y., Wang, Z., Zuo, X. & Gao, G. Electronic phase transition, spin filtering effect, and spin Seebeck effect in 2D high-spin-polarized VSi_2X_4 (X = N, P, As). *Appl. Phys. Lett.* **120**, 092405, doi:10.1063/5.0086990 (2022).

- 51 Akanda, M. R. K. & Lake, R. K. Magnetic properties of NbSi₂N₄, VSi₂N₄, and VSi₂P₄ monolayers. *Appl. Phys. Lett.* **119**, 052402, doi:10.1063/5.0055878 (2021).
- 52 Huang, B. *et al.* Layer-dependent ferromagnetism in a van der Waals crystal down to the monolayer limit. *Nature* **546**, 270–273, doi:10.1038/nature22391 (2017).
- 53 Fei, Z. *et al.* Two-dimensional itinerant ferromagnetism in atomically thin Fe₃GeTe₂. *Nature Mater.* **17**, 778–782, doi:10.1038/s41563-018-0149-7 (2018).
- 54 Abdelati, M. A., Maarouf, A. A. & Fadlallah, M. M. Substitutional transition metal doping in MoSi₂N₄ monolayer: structural, electronic and magnetic properties. *Physical Chemistry Chemical Physics* **24**, 3035–3042, doi:10.1039/d1cp04191f (2022).
- 55 Ding, Y. & Wang, Y. First-principles study of two-dimensional MoN₂X₂Y₂ (X=B~In, Y=N~Te) nanosheets: The III–VI analogues of MoSi₂N₄ with peculiar electronic and magnetic properties. *Appl. Surf. Sci.* **593**, 153317, doi:10.1016/j.apsusc.2022.153317 (2022).
- 56 Ray, A., Tyagi, S., Singh, N. & Schwingenschlögl, U. Inducing half-metallicity in monolayer MoSi₂N₄. *ACS Omega* **6**, 30371–30375, doi:10.1021/acsomega.1c03444 (2021).
- 57 Xiao, D., Chang, M.-C. & Niu, Q. Berry phase effects on electronic properties. *Rev. Mod. Phys.* **82**, 1959–2007, doi:10.1103/RevModPhys.82.1959 (2010).
- 58 Li, S. *et al.* Valley-dependent properties of monolayer MoSi₂N₄, WSi₂N₄, and MoSi₂As₄. *Phys. Rev. B* **102**, 235435, doi:10.1103/PhysRevB.102.235435 (2020).
- 59 Liu, Y. *et al.* Valley-contrasting physics in single-layer CrSi₂N₄ and CrSi₂P₄. *The Journal of Physical Chemistry Letters* **12**, 8341–8346, doi:10.1021/acs.jpcllett.1c02069 (2021).
- 60 Yuan, J. *et al.* Protected valley states and generation of valley- and spin-polarized current in monolayer MA₂Z₄. *Phys. Rev. B* **105**, 195151, doi:10.1103/PhysRevB.105.195151 (2022).
- 61 Yang, C., Song, Z., Sun, X. & Lu, J. Valley pseudospin in monolayer MoSi₂N₄ and MoSi₂As₄. *Phys. Rev. B* **103**, 035308, doi:10.1103/PhysRevB.103.035308 (2021).
- 62 Cui, Q., Zhu, Y., Liang, J., Cui, P. & Yang, H. Spin-valley coupling in a two-dimensional VSi₂N₄ monolayer. *Phys. Rev. B* **103**, 085421, doi:10.1103/PhysRevB.103.085421 (2021).
- 63 Zhou, X. *et al.* Sign-reversible valley-dependent Berry phase effects in 2D valley-half-semiconductors. *npj Comput. Mater.* **7**, 160, doi:10.1038/s41524-021-00632-3 (2021).
- 64 Li, S., Wang, Q., Zhang, C., Guo, P. & Yang, S. A. Correlation-driven topological and valley states in monolayer VSi₂P₄. *Phys. Rev. B* **104**, 085149, doi:10.1103/PhysRevB.104.085149 (2021).
- 65 Li, C. & Cheng, L. Intrinsic electron transport in monolayer MoSi₂N₄ and WSi₂N₄. *Journal of Applied Physics* **132**, 075111, doi:10.1063/5.0098837 (2022).
- 66 Qiu, X. *et al.* High hole mobilities in two dimensional monolayer MSi₂Z₄ (M = Mo/W; Z = P, As, Sb) for solar cells. *Journal of Materials Chemistry C* **10**, 15483–15490, doi:10.1039/d2tc03403d (2022).
- 67 Mortazavi, B., Shojaei, F., Javvaji, B., Rabczuk, T. & Zhuang, X. Outstandingly high thermal conductivity, elastic modulus, carrier mobility and piezoelectricity in two-dimensional semiconducting CrC₂N₄: a first-principles study. *Materials Today Energy* **22**, 100839, doi:10.1016/j.mtener.2021.100839 (2021).
- 68 Lv, X. *et al.* Dipole-regulated bandgap and high electron mobility for bilayer Janus MoSiGeN₄. *Appl. Phys. Lett.* **120**, 213101, doi:10.1063/5.0090481 (2022).
- 69 Ding, C.-H. *et al.* XMoSiN₂ (X = S, Se, Te): A novel 2D Janus semiconductor with ultra-high carrier mobility and excellent thermoelectric performance. *Europhysics Letters* **143**, 16002, doi:10.1209/0295-5075/acdb98 (2023).
- 70 Sun, X. *et al.* Performance limit of monolayer MoSi₂N₄ transistors. *Journal of Materials Chemistry C* **9**, 14683–14698, doi:10.1039/d1tc02937a (2021).
- 71 Ghobadi, N., Hosseini, M. & Touski, S. B. Field-effect transistor based on MoSi₂N₄ and WSi₂N₄ monolayers under biaxial strain: A computational study of the electronic properties. *IEEE Trans. Electron Devices* **69**, 863–869, doi:10.1109/ted.2021.3138377 (2022).

- 72 Shu, Y. *et al.* Efficient Ohmic contact in monolayer CrX_2N_4 ($X = \text{C}, \text{Si}$) based field-effect transistors. *Advanced Electronic Materials* **9**, 2201056, doi:10.1002/aelm.202201056 (2023).
- 73 Simmons. Generalized formula for the electric tunnel effect between similar electrodes separated by a thin insulating film. *Journal of Applied Physics* **34**, 1793–1803, 1963).
- 74 Matthews, N., Hagmann, M. J. & Mayer, A. Comment: “Generalized formula for the electric tunnel effect between similar electrodes separated by a thin insulating film” [J. Appl. Phys. **34**, 1793 (1963)]. *Journal of Applied Physics* **123**, 136101, doi:10.1063/1.5019788 (2018).
- 75 Wang, Q. *et al.* Efficient Ohmic contacts and built-in atomic sublayer protection in MoSi_2N_4 and WSi_2N_4 monolayers. *npj 2D Materials and Applications* **5**, 71, doi:10.1038/s41699-021-00251-y (2021).
- 76 Meng, Y. *et al.* Theoretical study on the electronic and transport properties of top and edge contact $\text{MoSi}_2\text{N}_4/\text{Au}$ heterostructure. *Physics Letters A* **456**, 128535, doi:10.1016/j.physleta.2022.128535 (2022).
- 77 Cao, L., Zhou, G., Wang, Q., Ang, L. K. & Ang, Y. S. Two-dimensional van der Waals electrical contact to monolayer MoSi_2N_4 . *Appl. Phys. Lett.* **118**, 013106, doi:10.1063/5.0033241 (2021).
- 78 Binh, N. T. T., Nguyen, C. Q., Vu, T. V. & Nguyen, C. V. Interfacial electronic properties and tunable contact types in graphene/Janus MoGeSiN_4 heterostructures. *The Journal of Physical Chemistry Letters* **12**, 3934–3940, doi:10.1021/acs.jpcclett.1c00682 (2021).
- 79 Ai, W., Shi, Y., Hu, X., Yang, J. & Sun, L. Tunable Schottky barrier and efficient Ohmic contacts in MSi_2N_4 ($M = \text{Mo}, \text{W}$)/2D metal contacts. *ACS Applied Electronic Materials* **5**, 5606–5613, doi:10.1021/acsaelm.3c00922 (2023).
- 80 Liu, H. *et al.* Giant tunnel magnetoresistance in two-dimensional van der Waals magnetic tunnel junctions: $\text{Ag}/\text{CrI}_3/\text{MoSi}_2\text{N}_4/\text{CrI}_3/\text{Ag}$. *Phys. Rev. B* **106**, 104429, doi:10.1103/PhysRevB.106.104429 (2022).
- 81 Wang, L. *et al.* Two-dimensional obstructed atomic insulators with fractional corner charge in the MA_2Z_4 family. *Phys. Rev. B* **106**, 155144, doi:10.1103/PhysRevB.106.155144 (2022).
- 82 Xu, Y. *et al.* Filling-enforced obstructed atomic insulators. *arXiv*, 2106.10276, doi:10.48550/arXiv.2106.10276 (2021).
- 83 Gong, Y. *et al.* Band gap engineering and layer-by-layer mapping of selenium-doped molybdenum disulfide. *Nano Lett.* **14**, 442–449, doi:10.1021/nl4032296 (2014).
- 84 Sun, M., Re Fiorentin, M., Schwingenschlögl, U. & Palummo, M. Excitons and light-emission in semiconducting MoSi_2X_4 two-dimensional materials. *npj 2D Materials and Applications* **6**, 81, doi:10.1038/s41699-022-00355-z (2022).
- 85 Yang, Y., Xie, L., Ma, Y. & Lu, H.-Y. Theoretical studies of valleytronic and optical properties in monolayer $\text{MoP}_2\text{X}_2\text{Y}_2$ ($\text{XY} = \text{BTe}, \text{AlS}, \text{and GaS}$). *Phys. Rev. B* **106**, 085412, doi:10.1103/PhysRevB.106.085412 (2022).
- 86 Li, Y. *et al.* The first-principle study on tuning optical properties of MA_2Z_4 by Cr replacement of Mo atoms in MoSi_2N_4 . *Nanomaterials* **12**, 2822, doi:10.3390/nano12162822 (2022).
- 87 Zhang, Y. *et al.* Engineering electronic structures and optical properties of a MoSi_2N_4 monolayer via modulating surface hydrogen chemisorption. *RSC Advances* **13**, 26475–26483, doi:10.1039/d3ra04428a (2023).
- 88 Liu, M.-Y., He, Y., Li, X. & Xiong, K. Tuning of the electronic and photocatalytic properties of Janus WSiGeZ_4 ($Z = \text{N}, \text{P}, \text{and As}$) monolayers via strain engineering. *Physical Chemistry Chemical Physics* **25**, 7278–7288, doi:10.1039/d2cp05224e (2023).
- 89 Selig, M. *et al.* Ultrafast dynamics in monolayer transition metal dichalcogenides: Interplay of dark excitons, phonons, and intervalley exchange. *Physical Review Research* **1**, 022007, doi:10.1103/PhysRevResearch.1.022007 (2019).
- 90 Aleithan, S. H. *et al.* Broadband femtosecond transient absorption spectroscopy for a CVD MoS_2 monolayer. *Phys. Rev. B* **94**, 035445, doi:10.1103/PhysRevB.94.035445 (2016).

- 91 Ai, H. *et al.* Theoretical evidence of the spin–valley coupling and valley polarization in two-dimensional MoSi_2X_4 ($\text{X} = \text{N}, \text{P}, \text{and As}$). *Physical Chemistry Chemical Physics* **23**, 3144–3151, doi:10.1039/d0cp05926a (2021).
- 92 Woźniak, T., Umm-e-hani, Faria Junior, P. E., Ramzan, M. S. & Kuc, A. B. Electronic and excitonic properties of MSi_2Z_4 monolayers. *Small* **19**, 2206444, doi:10.1002/smll.202206444 (2023).
- 93 Palummo, M., Bernardi, M. & Grossman, J. C. Exciton radiative lifetimes in two-dimensional transition metal dichalcogenides. *Nano Lett.* **15**, 2794–2800, doi:10.1021/nl503799t (2015).
- 94 Chen, H.-Y., Palummo, M., Sangalli, D. & Bernardi, M. Theory and ab Initio computation of the anisotropic light emission in monolayer transition metal dichalcogenides. *Nano Lett.* **18**, 3839–3843, doi:10.1021/acs.nanolett.8b01114 (2018).
- 95 Chen, H.-Y., Jhalani, V. A., Palummo, M. & Bernardi, M. Ab initio calculations of exciton radiative lifetimes in bulk crystals, nanostructures, and molecules. *Phys. Rev. B* **100**, 075135, doi:10.1103/PhysRevB.100.075135 (2019).
- 96 Zhong, H. *et al.* Exciton spectra and layer decomposition in $\text{MoSi}_2\text{N}_4/\text{WSi}_2\text{N}_4$ heterostructures. *Phys. Rev. B* **108**, 205131, doi:10.1103/PhysRevB.108.205131 (2023).
- 97 Mak, K. F. & Shan, J. Semiconductor moiré materials. *Nature Nanotechnology* **17**, 686–695, doi:10.1038/s41565-022-01165-6 (2022).
- 98 Du, L. New excitons in multilayer 2D materials. *Nature Reviews Physics* **6**, 157–159, doi:10.1038/s42254-024-00704-5 (2024).
- 99 Huang, D. *et al.* MoSi_2N_4 : A 2D regime with strong exciton–phonon coupling. *Advanced Optical Materials* **10**, 2102612, doi:https://doi.org/10.1002/adom.202102612 (2022).
- 100 Huang, D. *et al.* Exciton self-trapping effect in MoSi_2N_4 for modulating nonlinear optical process. *Advanced Optical Materials* **11**, 2202622, doi:10.1002/adom.202202622 (2023).
- 101 Liu, C., Wang, Z., Xiong, W., Zhong, H. & Yuan, S. Effect of vertical strain and in-plane biaxial strain on type-II $\text{MoSi}_2\text{N}_4/\text{Cs}_3\text{Bi}_2\text{I}_9$ van der Waals heterostructure. *Journal of Applied Physics* **131**, 163102, doi:10.1063/5.0080224 (2022).
- 102 Fang, L. *et al.* First-principles insights of electronic properties of Blue Phosphorus/ MoSi_2N_4 van der Waals heterostructure via vertical electric field and biaxial strain. *Physica E: Low-dimensional Systems and Nanostructures* **143**, 115321, doi:10.1016/j.physe.2022.115321 (2022).
- 103 Nguyen, C. Q. *et al.* Tunable type-II band alignment and electronic structure of $\text{C}_3\text{N}_4/\text{MoSi}_2\text{N}_4$ heterostructure: Interlayer coupling and electric field. *Phys. Rev. B* **105**, 045303, doi:10.1103/PhysRevB.105.045303 (2022).
- 104 Ng, J. Q., Wu, Q., Ang, L. K. & Ang, Y. S. Tunable electronic properties and band alignments of $\text{MoSi}_2\text{N}_4/\text{GaN}$ and $\text{MoSi}_2\text{N}_4/\text{ZnO}$ van der Waals heterostructures. *Appl. Phys. Lett.* **120**, 103101, doi:10.1063/5.0083736 (2022).
- 105 Xu, X. *et al.* Type-II $\text{MoSi}_2\text{N}_4/\text{MoS}_2$ van der Waals heterostructure with excellent optoelectronic performance and tunable electronic properties. *The Journal of Physical Chemistry C* **127**, 7878–7886, doi:10.1021/acs.jpcc.3c00773 (2023).
- 106 Cai, X. *et al.* A two-dimensional $\text{MoSe}_2/\text{MoSi}_2\text{N}_4$ van der Waals heterostructure with high carrier mobility and diversified regulation of its electronic properties. *Journal of Materials Chemistry C* **9**, 10073–10083, doi:10.1039/d1tc01149a (2021).
- 107 Wu, Q., Cao, L., Ang, Y. S. & Ang, L. K. Semiconductor-to-metal transition in bilayer MoSi_2N_4 and WSi_2N_4 with strain and electric field. *Appl. Phys. Lett.* **118**, 113102, doi:10.1063/5.0044431 (2021).
- 108 Pei, M. *et al.* Tuning the band alignment and electronic properties of $\text{XSe}_2/\text{WSi}_2\text{N}_4$ ($\text{X}=\text{Mo},\text{W}$) van der waals heterostructures with high carrier mobility. *Physica E: Low-dimensional Systems and Nanostructures* **149**, 115656, doi:10.1016/j.physe.2023.115656 (2023).
- 109 Nguyen, C., Hoang, N. V., Phuc, H. V., Sin, A. Y. & Nguyen, C. V. Two-dimensional Boron Phosphide/ MoGe_2N_4 van der Waals heterostructure: A promising tunable optoelectronic

- material. *The Journal of Physical Chemistry Letters* **12**, 5076–5084, doi:10.1021/acs.jpcllett.1c01284 (2021).
- 110 Wang, J., Zhao, X., Hu, G., Ren, J. & Yuan, X. Manipulable electronic and optical properties of two-dimensional MoSTe/MoGe₂N₄ van der Waals heterostructures. *Nanomaterials* **11**, 3338, doi:10.3390/nano11123338 (2021).
- 111 Zhang, Q.-K. *et al.* 2D Janus MoSSe/MoGeSiN₄ vdW heterostructures for photovoltaic and photocatalysis applications. *Journal of Alloys and Compounds* **938**, 168708, doi:10.1016/j.jallcom.2023.168708 (2023).
- 112 Tho, C. C. *et al.* MA2Z4 family heterostructures: Promises and prospects. *Applied Physics Reviews* **10**, 041307, doi:10.1063/5.0156988 (2023).
- 113 Bafekry, A. *et al.* A van der Waals heterostructure of MoS₂/MoSi₂N₄: a first-principles study. *New J Chem* **45**, 8291–8296, doi:10.1039/d1nj00344e (2021).
- 114 Cai, X., Zhang, Z., Chen, G., Wang, Q. & Jia, Y. Tunable electronic property and robust type-II feature in blue Phosphorene/MoSi₂N₄ bilayer heterostructure. *Crystals* **12**, 1407, doi:10.3390/cryst12101407 (2022).
- 115 Guo, Y. *et al.* Two-dimensional type-II BP/MoSi₂P₄ vdW heterostructures for high-performance solar cells. *The Journal of Physical Chemistry C* **126**, 4677–4683, doi:10.1021/acs.jpcc.1c10476 (2022).
- 116 Deng, D. *et al.* Catalysis with two-dimensional materials and their heterostructures. *Nature Nanotechnology* **11**, 218–230, doi:10.1038/nnano.2015.340 (2016).
- 117 Deng, J. *et al.* Multiscale structural and electronic control of molybdenum disulfide foam for highly efficient hydrogen production. *Nat. Commun.* **8**, 14430, doi:10.1038/ncomms14430 (2017).
- 118 Voiry, D., Yang, J. & Chhowalla, M. Recent strategies for improving the catalytic activity of 2D TMD nanosheets toward the hydrogen evolution reaction. *Adv. Mater.* **28**, 6197–6206, doi:https://doi.org/10.1002/adma.201505597 (2016).
- 119 Zhang, B., Zhou, J., Guo, Z., Peng, Q. & Sun, Z. Two-dimensional chromium boride MBenes with high HER catalytic activity. *Appl. Surf. Sci.* **500**, 144248, doi:10.1016/j.apsusc.2019.144248 (2020).
- 120 Twilton, J. *et al.* The merger of transition metal and photocatalysis. *Nature Reviews Chemistry* **1**, 0052, doi:10.1038/s41570-017-0052 (2017).
- 121 Peng, Q., Zhou, J., Chen, J., Zhang, T. & Sun, Z. Cu single atoms on Ti₂CO₂ as a highly efficient oxygen reduction catalyst in a proton exchange membrane fuel cell. *Journal of Materials Chemistry A* **7**, 26062–26070, doi:10.1039/c9ta08297b (2019).
- 122 Yu, Y., Zhou, J. & Sun, Z. Novel 2D transition-metal carbides: ultrahigh performance electrocatalysts for overall water splitting and oxygen reduction. *Adv. Funct. Mater.* **30**, 2000570, doi:10.1002/adfm.202000570 (2020).
- 123 Zhang, T., Zhang, B., Peng, Q., Zhou, J. & Sun, Z. Mo₂B₂ MBene-supported single-atom catalysts as bifunctional HER/OER and OER/ORR electrocatalysts. *Journal of Materials Chemistry A* **9**, 433–441, doi:10.1039/d0ta08630d (2021).
- 124 Wang, E., Zhang, B., Zhou, J. & Sun, Z. High catalytic activity of MBenes-supported single atom catalysts for oxygen reduction and oxygen evolution reaction. *Appl. Surf. Sci.* **604**, 154522, doi:10.1016/j.apsusc.2022.154522 (2022).
- 125 Liu, J. J., Fu, X. L., Chen, S. F. & Zhu, Y. F. Electronic structure and optical properties of Ag₃PO₄ photocatalyst calculated by hybrid density functional method. *Appl. Phys. Lett.* **99**, 191903, doi:10.1063/1.3660319 (2011).
- 126 Bartolotti, L. J., Gadre, S. R. & Parr, R. G. Electronegativities of the elements from simple Xa theory. *Journal of the American Chemical Society* **102**, 2945–2948, doi:10.1021/ja00529a013 (1980).
- 127 Nishioka, S., Osterloh, F. E., Wang, X., Mallouk, T. E. & Maeda, K. Photocatalytic water splitting. *Nature Reviews Methods Primers* **3**, 42, doi:10.1038/s43586-023-00226-x (2023).

- 128 Latimer, W. M. *Oxidation Potentials*. (Prentice Hall, 1952).
- 129 Jian, C.-c., Ma, X., Zhang, J. & Yong, X. Strained MoSi₂N₄ monolayers with excellent solar energy absorption and carrier transport properties. *The Journal of Physical Chemistry C* **125**, 15185–15193, doi:10.1021/acs.jpcc.1c03585 (2021).
- 130 Xu, J. *et al.* First-principles investigations of electronic, optical, and photocatalytic properties of Au-adsorbed MoSi₂N₄ monolayer. *Journal of Physics and Chemistry of Solids* **162**, 110494, doi:10.1016/j.jpcs.2021.110494 (2022).
- 131 Liu, Y., Jiang, Z., Jia, J., Robertson, J. & Guo, Y. 2D WSe₂/MoSi₂N₄ type-II heterojunction with improved carrier separation and recombination for photocatalytic water splitting. *Appl. Surf. Sci.* **611**, 155674, doi:10.1016/j.apsusc.2022.155674 (2023).
- 132 Xuefeng, C. *et al.* A direct Z-scheme MoSi₂N₄/BlueP vdW heterostructure for photocatalytic overall water splitting. *Journal of Physics D: Applied Physics* **55**, 215502, doi:10.1088/1361-6463/ac5662 (2022).
- 133 Sun, X. *et al.* DFT Investigation of single metal atom-doped 2D MA₂Z₄ Materials for NO electrocatalytic reduction to NH₃. *The Journal of Physical Chemistry C* **126**, 17598–17607, doi:10.1021/acs.jpcc.2c05780 (2022).
- 134 Lu, S., Zhang, Y., Lou, F., Guo, K. & Yu, Z. Non-precious metal activated MoSi₂N₄ monolayers for high-performance OER and ORR electrocatalysts: A first-principles study. *Appl. Surf. Sci.* **579**, 152234, doi:10.1016/j.apsusc.2021.152234 (2022).
- 135 Xun, W. *et al.* Single-atom-anchored two-dimensional MoSi₂N₄ monolayers for efficient electroreduction of CO₂ to Formic acid and methane. *ACS Applied Energy Materials* **6**, 3236–3243, doi:10.1021/acsaem.2c03687 (2023).
- 136 Sun, Z. *et al.* Alkali-metal(Li, Na, and K)-adsorbed MoSi₂N₄ monolayer: an investigation of its outstanding electronic, optical, and photocatalytic properties. *Communications in Theoretical Physics* **74**, 015503, doi:10.1088/1572-9494/ac3ada (2022).
- 137 Zhao, J. *et al.* Stacking engineering: A boosting strategy for 2D photocatalysts. *The Journal of Physical Chemistry Letters* **12**, 10190–10196, doi:10.1021/acs.jpcclett.1c03089 (2021).
- 138 Mwanemwa, N. *et al.* First principles calculations investigation of optoelectronic properties and photocatalytic CO₂ reduction of (MoSi₂N₄)_{5-n}/(MoSiGeN₄)_n in-plane heterostructures. *Results in Physics* **37**, 105549, doi:10.1016/j.rinp.2022.105549 (2022).
- 139 Zeng, J. *et al.* Boosting the photocatalytic hydrogen evolution performance of monolayer C₂N coupled with MoSi₂N₄: density-functional theory calculations. *Physical Chemistry Chemical Physics* **23**, 8318–8325, doi:10.1039/d1cp00364j (2021).
- 140 Li, R.-X. *et al.* MoSi₂N₄/CrS₂ van der Waals heterostructure with high solar-to-hydrogen efficiency. *Physica E: Low-dimensional Systems and Nanostructures* **144**, 115443, doi:10.1016/j.physe.2022.115443 (2022).
- 141 He, Y. *et al.* High hydrogen production in the InSe/MoSi₂N₄ van der Waals heterostructure for overall water splitting. *Physical Chemistry Chemical Physics* **24**, 2110–2117, doi:10.1039/d1cp04705a (2022).
- 142 Zhang, W., Yang, W., Liu, Y., Liu, Z. & Zhang, F. Computational exploration and screening of novel Janus MA₂Z₄ (M = Sc-Zn, Y-Ag, Hf-Au; A=Si, Ge; Z=N, P) monolayers and potential application as a photocatalyst. *Front. Phys.* **17**, 63509, doi:10.1007/s11467-022-1199-5 (2022).
- 143 Xiao, C. *et al.* Adsorption behavior of environmental gas molecules on pristine and defective MoSi₂N₄: Possible application as highly sensitive and reusable gas sensors. *ACS Omega* **7**, 8706–8716, doi:10.1021/acsomega.1c06860 (2022).
- 144 Bafekry, A. *et al.* Adsorption of habitat and industry-relevant molecules on the MoSi₂N₄ monolayer. *Appl. Surf. Sci.* **564**, 150326, doi:10.1016/j.apsusc.2021.150326 (2021).
- 145 Merchant, A. *et al.* Scaling deep learning for materials discovery. *Nature* **624**, 80–85, doi:10.1038/s41586-023-06735-9 (2023).

- 146 Hippalgaonkar, K. *et al.* Knowledge-integrated machine learning for materials: lessons from
gameplaying and robotics. *Nature Reviews Materials* **8**, 241–260, doi:10.1038/s41578-022-
00513-1 (2023).
- 147 Kazeev, N. *et al.* Sparse representation for machine learning the properties of defects in 2D
materials. *npj Comput. Mater.* **9**, 113, doi:10.1038/s41524-023-01062-z (2023).
- 148 Huang, P. *et al.* Unveiling the complex structure-property correlation of defects in 2D
materials based on high throughput datasets. *npj 2D Materials and Applications* **7**, 6,
doi:10.1038/s41699-023-00369-1 (2023).
- 149 Sun, Y. *et al.* Accelerating the discovery of transition metal Borides by machine learning on
small data sets. *ACS Appl. Mater. Interfaces* **15**, 29278–29286, doi:10.1021/acsami.3c03657
(2023).

Supplementary Information for

MoSi₂N₄-like crystals – the new family of two-dimensional materials

T. Latychevskaia¹, D. Bandurin^{2*}, K. S. Novoselov^{3*}

¹Paul Scherrer Institute, Forschungsstrasse 111, 5232 Villigen, Switzerland

²Department of Materials Science and Engineering, National University of Singapore, Singapore, 117575, Singapore

³Institute for Functional Intelligent Materials, National University of Singapore, Building S9, 4 Science Drive 2, Singapore 117544

*E-mail: dab@nus.edu.sg; kostya@nus.edu.sg

Contents

1. MA ₂ Z ₄ structures	2
2. MA ₂ Z ₄ -metal structures	3
2.1 Tunnelling probability	3
2.2 Specific resistivity	3
2.3 Summary of electronic properties of MA ₂ Z ₄ -metal structures.....	4
2. MA ₂ Z ₄ -semiconductor hetrostructures.....	7
3. Catalytic properties of MA ₂ Z ₄ materials	10
References	12

1. MA₂Z₄ structures

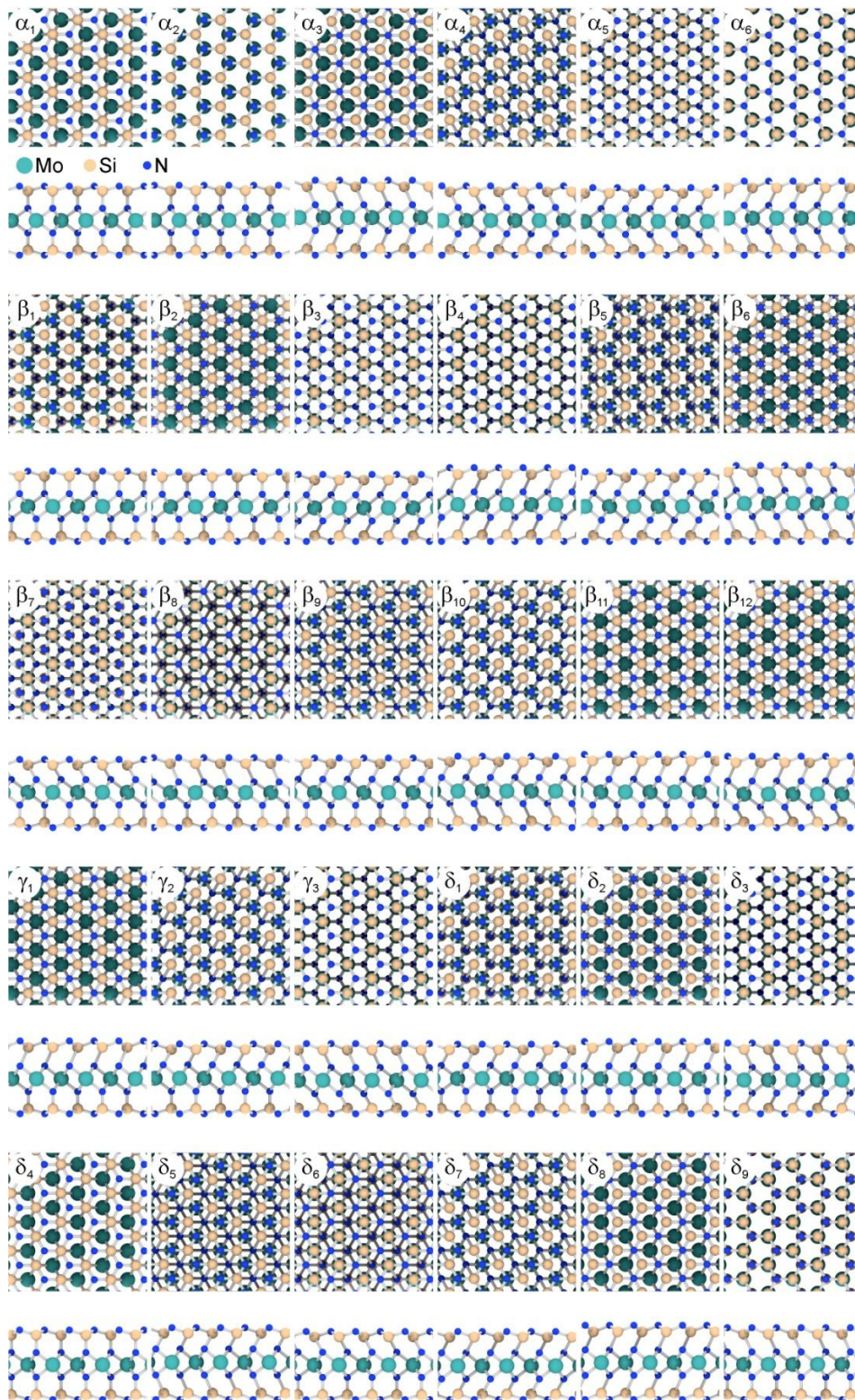


Fig. S1. 30 possible structures of MA₂Z₄ calculated for MoSi₂N₄, using atomic coordinates provided in ref. [1] ([Wang2021NatCommun](#)); top and side views for each structure.

2. MA₂Z₄-metal structures

2.1 Tunnelling probability

The tunnelling probability of a particle with energy E through a potential barrier $V(x)$ can be calculated as:

$$T(E) = \exp\left\{-2\int_{x_1}^{x_2} \sqrt{\frac{2m_e}{\hbar^2} [V(x) - E]} dx\right\} \approx \exp\left[-2w\sqrt{\frac{2m_e}{\hbar^2} (V_0 - E)}\right], \quad (S1)$$

where a rectangular barrier of height V_0 and width w is assumed, m_e is the free-electron mass and \hbar is the reduced Planck's constant. The tunnelling probability through the Schottky barrier is given by

$$P_{\text{TB}}(w_{\text{TB}}, \Phi_{\text{TB}}) = \exp\left(-2w_{\text{TB}} \frac{\sqrt{2m_e \Phi_{\text{TB}}}}{\hbar}\right) = \exp(-2w_{\text{TB}} k_{\text{TB}}), \quad (S2)$$

where Φ_{TB} and w_{TB} are the height and width of the barrier, $k_{\text{TB}} = \sqrt{2m_e \Phi_{\text{TB}}} / \hbar$ is the wavenumber.

2.2 Specific resistivity

The relationship between the current density and voltage in a tunnel junction is given by Eq. (20) in ref.[2] (Simmons1963JAP_p1793)

$$J_{\text{TB}} = \frac{e}{2\pi\hbar w_{\text{TB}}^2} \left\{ \bar{\varphi} \exp(-A\bar{\varphi}^{1/2}) - (\bar{\varphi} + eV) \exp\left[-A(\bar{\varphi} + eV)^{1/2}\right] \right\}, \quad (S3)$$

where $\bar{\varphi}$ is the mean value of the barrier height above the Fermi level of the negatively biased electrode, V is the applied voltage, e is the electron charge, and

$$A = \frac{4\pi w_{\text{TB}}}{\hbar} (2m_e)^{1/2} = \frac{2w_{\text{TB}}}{\hbar} (2m_e)^{1/2}. \quad (S4)$$

At the intermediate voltages, the mean barrier height is given by

$$\bar{\varphi} = \frac{\varphi_1 + \varphi_2 - eV}{2}, \quad (S5)$$

and for $\varphi_1 = \varphi_2 = \Phi_{\text{TB}}$, Eq. (S3) becomes:

$$J_{\text{TB}} = \frac{e}{4\pi^2 \hbar w_{\text{TB}}^2} \times \left\{ \left(\Phi_{\text{TB}} - \frac{eV}{2} \right) \exp\left(-2w_{\text{TB}} \frac{\sqrt{2m_e (\Phi_{\text{TB}} - eV/2)}}{\hbar}\right) - \left(\Phi_{\text{TB}} + \frac{eV}{2} \right) \exp\left[-2w_{\text{TB}} \frac{\sqrt{2m_e (\Phi_{\text{TB}} + eV/2)}}{\hbar}\right] \right\} \quad (S6)$$

The tunnelling resistivity is calculated as:

$$\rho_{\text{TB}}(w_{\text{TB}}, \Phi_{\text{TB}}) = \left(\frac{dJ_{\text{TB}}}{dV} \right)^{-1} \Bigg|_{V=0} = \frac{4\pi^2 \hbar w_{\text{TB}}^2}{e^2} \frac{\exp(2w_{\text{TB}} k_{\text{TB}})}{w_{\text{TB}} k_{\text{TB}} - 1}. \quad (S7)$$

For thin barriers, Eq. (S7) gives unphysical negative values, and instead, a low-voltage ($eV \approx 0$) approximation is used. For low voltages, Eq. (S3) reduces to

$$J_{\text{TB}} = \frac{e^2 (2m_e \bar{\varphi})^{1/2}}{4\pi^2 \hbar^2 w_{\text{TB}}} V \exp\left(-2w_{\text{TB}} \frac{(2m_e \bar{\varphi})^{1/2}}{\hbar}\right), \quad (\text{S8})$$

and substituting

$$\bar{\varphi} = \frac{\varphi_1 + \varphi_2}{2} = \Phi_{\text{TB}} \quad (\text{S9})$$

gives

$$J_{\text{TB}} = \frac{e^2 (2m_e \Phi_{\text{TB}})^{1/2}}{4\pi^2 \hbar^2 w_{\text{TB}}} V \exp\left(-2w_{\text{TB}} \frac{(2m_e \Phi_{\text{TB}})^{1/2}}{\hbar}\right), \quad (\text{S10})$$

The tunnelling resistivity is calculated as:

$$\rho_{\text{TB}}(w_{\text{TB}}, \Phi_{\text{TB}}) = \left(\frac{dJ_{\text{TB}}}{dV}\right)^{-1} \Bigg|_{V=0} = \frac{4\pi^2 \hbar^2 w_{\text{TB}}}{e^2 (2m_e \Phi_{\text{TB}})^{1/2}} \exp\left(2w_{\text{TB}} \frac{(2m_e \Phi_{\text{TB}})^{1/2}}{\hbar}\right), \quad (\text{S11})$$

note that the result in Eq. (S11) is different from the result obtained by Simmons by factor 2/3, the issue has been previously discussed in ref.[3] (Matthews2018JAP).

2.3 Summary of electronic properties of MA₂Z₄-metal structures

Table S1. Properties of MA₂Z₄-metal systems. "G"=graphene. n-type and p-type are highlighted in blue and pink, Schottky and Ohmic - in weak and strong color, respectively. The tunnelling barrier probability and resistivity were calculated in this study by using Eqs. (S2) and (S7), respectively. When the resistivity by Eq. (S7) was negative, it was re-calculated by Eq. (S11) (highlighted in lilac). LM - lattice mismatch (copied from the cited papers), d_0 - interlayer distance, EF - the electric field.

Composition	Schottky barrier height		tunneling barrier			Resistivity 10 ⁻⁹ Ohm·cm ²	LM %	$d_0/\text{Å}$	strain		EF	reference
	Φ_{Bn} eV	Φ_{Bp} eV	height eV	width Å	probability %				vertical	biaxial		
MoSi₂N₄												
G	1.027	0.979	NA	NA	NA	NA	2.39	3.35	NA	p to n at $\varepsilon < -2\%$, to Ohmic at $\varepsilon < -10\%$	NA	[4]
G	0.922	0.797	NA	NA	NA	NA	1.6	3.302	p to n at $d > 3.5\text{Å}$	NA	p to n at EF > 0.05V/Å	[5]
G	1.49	0.96	NA	NA	NA	NA	1.65	3.16	NA	NA	NA	[6]
G	1.03	0.98	4.04	1.92	1.917	3.191	2.39	3.35	NA	NA	NA	[7]
G	0.68	0.97	9.98	1.30	1.488	1.669	1.59	3.18	n to p at $d < 2.89\text{Å}$	NA	n to p at EF > 0.06 V/Å, to Ohmic at EF > 0.8 V/Å and EF < 0.6 V/Å	[8]
G	1.14	1.06	NA	NA	NA	NA	1.70	3.36	p to n at $d > 3.4\text{Å}$	NA	p to n at EF > 0, Ohmic at EF > 0.3V/Å and EF < 0.3V/Å	[9]
G	1.28	0.38	4.45	1.96	1.446	3.854	1.60	3.33	NA	NA	NA	[10]
G	NA	0.95	NA	NA	NA	NA	1.07	3.30	NA	NA	NA	[11]
Hf ₄ C ₃	-0.915	2.711	0.000	0.000	100	0.000	1.5	2.25	NA	NA	NA	[12]
Hf ₄ C ₃ F ₂	-0.118	1.921	2.304	1.283	13.596	0.197	1.8	2.55	NA	NA	NA	[12]
Hf ₄ C ₃ O ₂	1.500	0.543	3.981	1.493	4.725	1.454	1.2	2.65	NA	NA	NA	[12]
Hf ₄ C ₃ O ₂ H ₂	0.543	2.174	0.419	0.487	72.397	0.033	1.2	1.80	NA	NA	NA	[12]
1T-MoS ₂	NA	0.76	NA	NA	NA	NA	2.61	3.20	NA	NA	NA	[11]
MoSH	0.54	0.50	NA	NA	NA	NA	1.70	2.90	p to n at $\Delta d < 0.1\text{Å}$, to Ohmic at $\Delta d < 1.2\text{Å}$	NA	p to n at EF > 0 V/nm, to Ohmic at EF < -0.35 V/nm	[13]
MoHS	0.90	0.11	NA	NA	NA	NA	1.70	3.32	NA	NA	p to n at EF > 0.3 V/nm, to Ohmic at EF < -0.3 V/nm	[13]
NbS ₂	NA	-0.08	NA	NA	NA	NA	0.19	3.10	NA	NA	NA	[11]
NbS ₂	1.642	0.042	NA	NA	NA	NA	0.07	3.192	remains p	NA	p to Ohmic at EF < -0.2 V/Å	[5]
NbS ₂	1.87	-0.04	5.21	1.93	1.096	4.387	0.85	3.18	NA	NA	NA	[7]
NbS ₂	1.65	-0.03	5.14	1.88	1.269	3.818	0.14	3.15	NA	NA	NA	[10]
NbSe ₂	NA	-0.01	NA	NA	NA	NA	1.77	3.20	NA	NA	NA	[11]
NbSe ₂	1.63	0.09	4.74	1.87	1.543	3.386	3.69	3.26	NA	NA	NA	[7]

Ag	0.67	1.37	3.01	1.42	8.011	1.557	0.55	3.09	NA	NA	NA	[10]
Au	1.44	0.68	3.73	1.48	5.346	1.431	0.68	3.13	NA	NA	NA	[10]
Cu	0.65	1.48	2.80	1.23	12.137	3.713	0.88	2.82	NA	NA	NA	[10]
In	0.43	1.59	2.94	1.69	5.135	1.862	1.53	3.42	NA	NA	NA	[10]
Ni	0.82	1.13	2.08	1.29	14.863	0.191	0.82	2.38	NA	NA	NA	[10]
Sc	-0.06	2.03	0.00	0.00	100	0.000	1.11	2.33	NA	NA	NA	[10]
Ti	-0.12	2.06	0.00	0.00	100	0.000	0.85	1.78	NA	NA	NA	[10]
Pd	1.14	0.97	2.98	1.13	13.551	0.153	3.72	2.71	NA	NA	NA	[10]
Pt	1.85	0.20	4.04	1.46	4.945	1.389	3.18	3.02	NA	NA	NA	[10]
CrSi₂N₄												
G	0.03	0.45	4.35	1.89	1.761	3.226	0.15	3.35	NA	NA	NA	[17]
Ag	-0.03	0.54	2.91	1.30	10.308	1.953	0.04	2.79	NA	NA	NA	[17]
Au	0.02	0.54	3.69	1.44	5.876	1.372	0.19	3.02	NA	NA	NA	[17]
Cu	-0.03	0.52	2.79	1.09	15.482	0.133	0.55	2.62	NA	NA	NA	[17]
Ni	-0.01	0.60	3.17	1.20	11.201	2.204	0.62	2.67	NA	NA	NA	[17]
Pd	-0.02	0.74	2.00	0.80	31.372	0.057	1.35	2.40	NA	NA	NA	[17]
Pt	-0.01	0.75	2.99	1.08	14.756	0.134	1.75	2.69	NA	NA	NA	[17]
Ti	-0.04	0.58	2.04	1.03	22.149	0.103	0.09	2.93	NA	NA	NA	[17]
CrC₂N₄												
G	0.05	1.85	4.08	1.69	3.027	2.044	1.65	3.22	NA	NA	NA	[17]
Ag	0.07	1.84	3.52	1.51	5.487	1.493	1.10	3.15	NA	NA	NA	[17]
Au	0.32	1.54	4.10	1.55	4.012	1.598	1.36	3.18	NA	NA	NA	[17]
Cu	-0.06	1.79	1.24	0.60	50.430	0.034	2.23	2.32	NA	NA	NA	[17]
Ni	0.15	1.81	0.32	0.13	92.742	0.000	1.17	2.05	NA	NA	NA	[17]
Pd	0.14	1.81	3.64	1.30	7.876	1.286	3.92	2.80	NA	NA	NA	[17]
Pt	0.19	1.73	3.69	1.22	9.060	1.328	3.29	2.77	NA	NA	NA	[17]
Ti	-0.13	1.75	0.00	0.00	100	0.000	1.14	2.31	NA	NA	NA	[17]

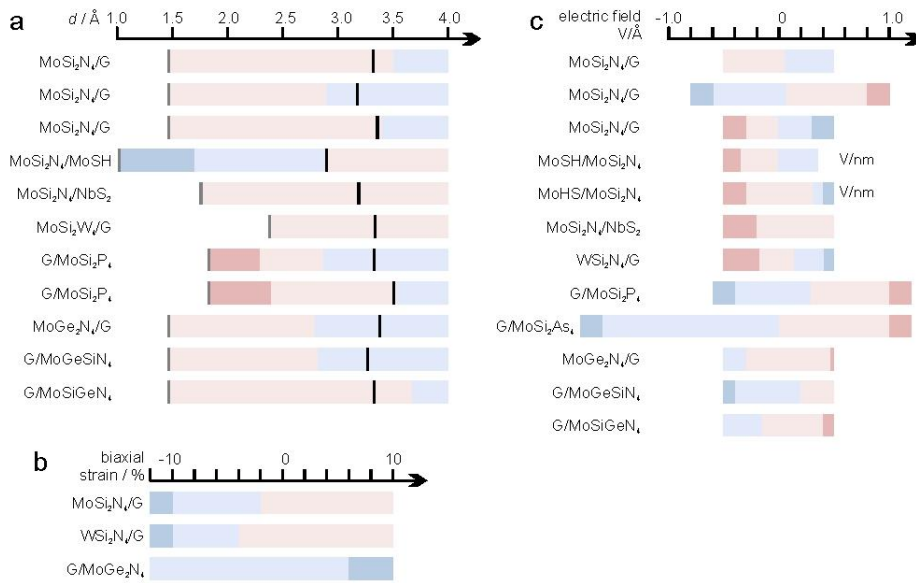


Fig. S2. Type of MA₂Z₄-metal structure as a function of **a**, vertical stress (interlayer distance), **b**, biaxial strain and **c**, electric field according to the data in **Table S1**. n-type and p-type are highlighted in blue and pink, Schottky and Ohmic - in weak and strong color, respectively. In **a**, the black vertical lines indicate the positions of the interlayer distance without vertical stress. The gray vertical lines indicate the positions of the minimal interlayer distance given by the sum of the covalent radii.

2. MA₂Z₄-semiconductor hetrostructures

Table S2. MA₂Z₄ - semiconductor (SC) heterostructures. BT - bandgap type (d - direct, i - indirect), BAL - band alignment type (I, II, III or h - hybrid). E_g is the energy gap, ML - monolayer, H - heterostructure, EF - electric field, LM - lattice mismatch, d - interlayer distance.

composition	BT	BAL	E_g / eV PBE	E_g / eV HSE	lattice constant		LM %	d / Å	strain vertical	strain biaxial	EF	reference
					ML / Å	H / Å						
MoSi₂N₄												
BlueP/MoSi ₂ N ₄	i	II	1.13	2.02	3.25/2.90	5.77	3	3.49		II to I at $\epsilon < 6\%$ II to I at $\epsilon > 8\%$	to metal at EF < 0.5V/Å and EF > 0.5V/Å II to I at EF > 0.3V/Å	[18]
MoSi ₂ N ₄ /BlueP	d	II	1.175	2	2.90/3.27	5.8	2.4	3.49	NA	$\epsilon = 0-8\%$, shifted absorption spectra	NA	[19]
MoSi ₂ N ₄ /BP	d	I	0.95	NA	NA	5.7	2.25	3.5	NA	NA	NA	[11]
C ₂ N/MoSi ₂ N ₄	d	II	NA	1.74	8.25/2.90	8.47	<3	NA	NA	NA	NA	[20]
C ₃ N ₄ /MoSi ₂ N ₄	d	II	1.86	2.66	4.78/2.90	4.94	2.8	3.65	II to I at $d = 2.65\text{Å}$	II to I at $\epsilon < 2\%$ I to II at $\epsilon < 5\%$ II to I at $\epsilon > 4\%$ d to i at $\epsilon > 5\%$	II to I at EF < 0.4 V/Å	[21]
MoSi ₂ N ₄ /CrCl ₃ (A stacking)	i	II	NA	NA	2.91/5.932	5.8	0.29	3.198		NA	NA	[22]
MoSi ₂ N ₄ /CrCl ₃ (B stacking)	i	II	NA	NA	2.91/5.932	5.8	0.29	3.212		NA	NA	[22]
MoSi ₂ N ₄ /CrS ₂	i	II	0.99	1.52	2.909/3.039	2.924	4.37	3.151	remains type II	II to I at $\epsilon < 1.4\%$	NA	[23]
MoSi ₂ N ₄ /Cs ₃ Bi ₂ I ₉	d	II	0.91	NA	2.90/8.65	8.66	0.227	3.55	d to i at $d < 2.55\text{Å}$	d to i at $\epsilon < 8\%$ and $\epsilon > 10\%$, SC to metal at $\epsilon < 12\%$	NA	[24]
MoSi ₂ N ₄ /GaN	d	II	1.7	NA	NA	5.7	2.28	3.3	NA	NA	NA	[11]
MoSi ₂ N ₄ /GaN	d	I	1.56	NA	NA	NA	2.68	3.44	d, I to i, II at $d < 3.25\text{Å}$	NA	d to i at EF < 0 i to d at EF < 0.6V/Å	[25]
MoSi ₂ N ₄ /hBN	d	I	1.66	NA	NA	5	0.14	3.3	NA	NA	NA	[11]
MoSi ₂ N ₄ /InSe	d	II	1.62	NA	NA	7.7	2.96	3.3	NA	NA	NA	[11]
InSe/MoSi ₂ N ₄	d	II	1.35	1.61(GGA- 1/2)	4.08/2.91	10.48	2.84	3.326	NA	NA	NA	[26]
MoSi ₂ N ₄ /MoGe ₂ N ₄	i	II	0.37	NA	NA	1.5	1.86	2.7	NA	NA	NA	[11]
MoGe ₂ N ₄ /MoSi ₂ N ₄	i	II	0.88- 0.90	1.29-1.33	NA/NA	2.96	NA	3.33- 3.35	NA	NA	NA	[6]
MoSi ₂ N ₄ /α ₂ - MoGe ₂ P ₄	d	II	0.66	NA	NA	6	2.62	3.2	NA	NA	NA	[11]
MoSi ₂ N ₄ /MoS ₂	i	II	1.12	NA	2.91/3.18	2.96	4.43	3.11	NA	II to I at $\epsilon < 3\%$ and $\epsilon > 1\%$	II to I at EF < 0.2V/Å I to II at EF < 0.3V/Å II to III at EF < 0.5V/Å and EF > 0.4V/Å	[27]
MoS ₂ /MoSi ₂ N ₄	i	II	1.26	1.84	3.21/2.91	2.96	NA	3.21	NA	NA	NA	[28]
2H-MoSi ₂ N ₄ /MoS ₂	i	II	NA	2.08	2.902/3.18	2.96	NA	NA	NA	NA	NA	[29]
2H ⁻ -MoSi ₂ N ₄ /MoS ₂	i	II	NA	1.93	2.91/3.18	2.96	NA	NA	NA	NA	NA	[29]
MoSi ₂ N ₄ /2H-MoS ₂	d	h	0.6	NA	NA	5.7	2.69	3.2	NA	NA	NA	[11]
MoSi ₂ N ₄ /MoSe ₂	d	I	1.37	NA	NA	5.8	0.58	3.3	NA	NA	NA	[11]
MoSe ₂ /MoSi ₂ N ₄	d	I	1.39	1.82	3.3/2.9	5.78	1.4	3.29	NA	d to i at $\epsilon < 2\%$ I to II at $\epsilon < 7\%$ and $\epsilon > 1\%$	d, I to i, II at EF < 0.2 V/Å to d, II at EF > 0.04 V/Å	[30]
2H-MoSi ₂ N ₄ /MoSse	i	II	NA	1.26	2.902/3.25	2.97	NA	NA	NA	NA	NA	[29]
2H ⁻ -MoSi ₂ N ₄ / MoSse	i	I	NA	1.55	2.91/3.25	2.98	NA	NA	NA	NA	NA	[29]
MoSi ₂ N ₄ /MoSi ₂ N ₄	i	NA	1.64	2.22	2.9/2.9	2.9	0	NA	NA	i to d at $\epsilon < 4\%$	to metal at EF > 6V/nm	[31]
MoSi ₂ N ₄ /MoTe ₂	i	I	0.87	NA	NA	5.8	2.09	3.4	NA	NA	NA	[11]
MoSi ₂ N ₄ /Na ₃ Bi	NA	III	NA	NA	NA	5.2	2.04	1.4	NA	NA	NA	[11]
MoSi ₂ N ₄ /SMoSe	d	h	0.88	NA	NA	5.7	1.64	3.2	NA	NA	NA	[11]
MoSi ₂ N ₄ /SWSe	d	I	1.13	NA	NA	5.7	1.61	3.2	NA	NA	NA	[11]
MoSi ₂ N ₄ /SeMoS	d	I	1.13	NA	NA	5.7	1.64	3.3	NA	NA	NA	[11]
MoSi ₂ N ₄ /SeWS	d	I	1.17	NA	NA	5.7	1.61	3.3	NA	NA	NA	[11]
MoSi ₂ N ₄ /TiSi ₂ N ₄	i	NA	0	0.343	NA/NA	5.841	NA	NA	NA	to metal at $\epsilon < 4\%$		[32]
MoSi ₂ N ₄ /WGe ₂ N ₄	i	II	0.99	NA	NA	1.5	1.89	2.8	NA	NA	NA	[11]
MoSi ₂ N ₄ /α ₂ -WGe ₂ P ₄	d	h	0.78	NA	NA	6	2.1	3.2	NA	NA	NA	[11]
MoSi ₂ N ₄ /2H-WS ₂	d	I	1.05	NA	NA	5.7	2.64	3.2	NA	NA	NA	[11]
MoSi ₂ N ₄ /WSe ₂	i	II	1.4	NA	NA	5.8	1.09	3.3	NA	NA	NA	[11]
WSe ₂ /MoSi ₂ N ₄	i	II	1.38	1.81	3.3/2.90	5.8	NA	3.25	NA	NA	NA	[33]
WSe ₂ /MoSi ₂ N ₄	d	I	1.17	1.57	3.29/2.9	5.78	1.4	3.29	NA	NA	d, I to i, II at EF < 0.05V/Å; to d, II at EF > 0.4 V/Å	[34]
MoSi ₂ N ₄ /WSi ₂ N ₄	d	II	1.36	NA	NA	1.4	0.05	3	NA	NA	NA	[11]
MoSi ₂ N ₄ /WSi ₂ N ₄	i	NA	1.92	2.35	NA/NA	5.824	NA	NA	NA	i to d at $\epsilon < 3\%$		[32]
WSi ₂ N ₄ /MoSi ₂ N ₄	i	II	NA	1.9	2.915/2.909	2.902	~0	3.01	NA	NA	NA	[35]
MoSi ₂ N ₄ /WTe ₂	i	I	1.09	NA	NA	5.8	2.18	3.4	NA	NA	NA	[11]
MoSi ₂ N ₄ /ZnO	i	II	1.61	NA	NA	5.8	1.04	3.6	NA	NA	NA	[11]

MoSi ₂ N ₄ /ZnO	i	II	1.6	NA	NA	NA	0.92	3.15	i,II to d,I at $d>3.7\text{\AA}$	NA	i to d at $EF>0.2\text{V}/\text{\AA}$ i to d at $EF<-0.6\text{V}/\text{\AA}$	[25]
WSi₂N₄												
WSi ₂ N ₄ /BP	d	I	0.96	NA	NA	5.7	2.3	3.5	NA	NA	NA	[11]
WSi ₂ N ₄ /GaN	d	I	1.84	NA	NA	5.7	2.34	3.3	NA	NA	NA	[11]
WSi ₂ N ₄ /hBN	d	I	2.04	NA	NA	5	0.2	3.3	NA	NA	NA	[11]
WSi ₂ N ₄ /InSe	d	II	1.43	NA	NA	7.7	2.91	3.3	NA	NA	NA	[11]
WSi ₂ N ₄ /MoGe ₂ N ₄	i	II	0.25	NA	NA	1.5	1.8	2.8	NA	NA	NA	[11]
WSi ₂ N ₄ /α ₂ -MoGe ₂ P ₄	d	II	0.44	NA	NA	6	2.57	3.2	NA	NA	NA	[11]
WSi ₂ N ₄ /2H-MoS ₂	d	h	0.81	NA	NA	5.7	2.74	3.2	NA	NA	NA	[11]
MoSe ₂ /WSi ₂ N ₄	d	I	1.26	NA	NA	NA	0.82	3.25	I to II at $d>4\text{\AA}$	I to II at $\epsilon>1\%$ d to i at $\epsilon\leq 2\%$	I to II at $EF<-0.025\text{V}/\text{\AA}$ and $EF>0.075\text{V}/\text{\AA}$ II to III at $EF<-0.125\text{V}/\text{\AA}$ and $EF>0.2\text{V}/\text{\AA}$	[36]
WSi ₂ N ₄ /MoSe ₂	d	II	1.11	NA	NA	5.8	0.63	3.3	NA	NA	NA	[11]
WSi ₂ N ₄ /MoTe ₂	i	I	0.89	NA	NA	5.8	2.04	3.5	NA	NA	NA	[11]
WSi ₂ N ₄ /Na ₃ Bi	NA	III	NA	NA	NA	5.2	1.98	1.4	NA	NA	NA	[11]
WSi ₂ N ₄ /SMoSe	d	II	0.73	NA	NA	5.7	1.69	3.2	NA	NA	NA	[11]
WSi ₂ N ₄ /SeMoS	d	I	1.11	NA	NA	5.7	1.69	3.3	NA	NA	NA	[11]
WSi ₂ N ₄ /SeWS	d	I	1.28	NA	NA	5.7	1.67	3.3	NA	NA	NA	[11]
WSi ₂ N ₄ /SWSe	d	h	1.02	NA	NA	5.7	1.67	3.2	NA	NA	NA	[11]
WSi ₂ N ₄ /WGe ₂ N ₄	i	II	0.78	NA	NA	1.5	1.84	2.8	NA	NA	NA	[11]
WSi ₂ N ₄ /α ₂ -WGe ₂ P ₄	d	II	0.59	NA	NA	6	2.05	3.2	NA	NA	NA	[11]
WSi ₂ N ₄ /2H-WS ₂	d	I	1.04	NA	NA	5.7	2.69	3.2	NA	NA	NA	[11]
WSi ₂ N ₄ /WSe ₂	d	I	1.45	NA	NA	5.8	1.67	3.3	NA	NA	NA	[11]
WSe ₂ /WSi ₂ N ₄	d	I	1.16	NA	NA	NA	0.64	3.27	remains type I	I to II at $\epsilon>3\%$ d to i at $\epsilon\leq 2\%$	I to II at $EF<-0.05\text{V}/\text{\AA}$ and $EF>0.05\text{V}/\text{\AA}$ II to III at $EF<-0.2\text{V}/\text{\AA}$ and $EF>0.175\text{V}/\text{\AA}$	[36]
WSi ₂ N ₄ /WSi ₂ N ₄	i	NA	1.94	2.56	2.9/2.9	2.9	0	NA	NA	NA	to metal at $EF>6\text{V}/\text{nm}$	[31]
WSi ₂ N ₄ /WTe ₂	i	I	1.19	NA	NA	6	2.13	3.5	NA	NA	NA	[11]
WSi ₂ N ₄ /ZnO	d	I	1.83	NA	NA	5.8	1.1	3.1	NA	NA	NA	[11]
BP/MoSi₂P₄												
BP/MoSi ₂ P ₄	d	II	NA	1.02	3.21/3.47	NA	3.9	3.39	NA	NA	NA	[37]
BP/MoGe ₂ P ₄	d	II	0.34-0.47	0.62-0.77	3.2/3.04	3.12	2.56	3.08-3.38	II to I at $d<2.7\text{\AA}$	NA	II to I at $EF>0.15\text{V}/\text{\AA}$	[38]
(MoSi ₂ N ₄) ₅ / (MoSiGeN ₄) ₀	i	NA	1.925	2.385	NA/2.96	2.91	NA	NA	NA	NA	NA	[39]
(MoSi ₂ N ₄) ₄ / (MoSiGeN ₄) ₁	i	NA	1.823	2.71	NA/2.96	NA	NA	NA	NA	NA	NA	[39]
(MoSi ₂ N ₄) ₃ / (MoSiGeN ₄) ₂	i	NA	1.716	2.137	NA/2.96	NA	NA	NA	NA	NA	NA	[39]
(MoSi ₂ N ₄) ₂ / (MoSiGeN ₄) ₃	i	NA	1.598	2.021	NA/2.96	2.93	NA	NA	NA	NA	NA	[39]
(MoSi ₂ N ₄) ₁ / (MoSiGeN ₄) ₄	i	NA	1.494	1.979	NA/2.96	NA	NA	NA	NA	NA	NA	[39]
(MoSi ₂ N ₄) ₀ / (MoSiGeN ₄) ₅	i	NA	1.385	1.86	NA/2.96	2.9	NA	NA	NA	NA	NA	[39]
T ₄ -MoTe/ MoGe ₂ N ₄	NA	NA	0	NA	3.362/3.037	NA	1.48	3.4	to i gap SC at $d>3.63\text{\AA}$	semi-metal so SC at $\epsilon<-2\%$	NA	[40]
S ₄ -MoTe/ MoGe ₂ N ₄	d	II	0.27	NA	3.362/3.037	NA	1.48	3.1	no gap at $d<2.3\text{\AA}$	SC to semi-metal at $\epsilon>2\%$	NA	[40]
MoSse/MoGeSiN ₄	d	II	0.87	1.28	3.25/2.96	8.98	3.3	3.29		d to i at $\epsilon<-2\%$ no gap at $\epsilon>8\%$	NA	[41]

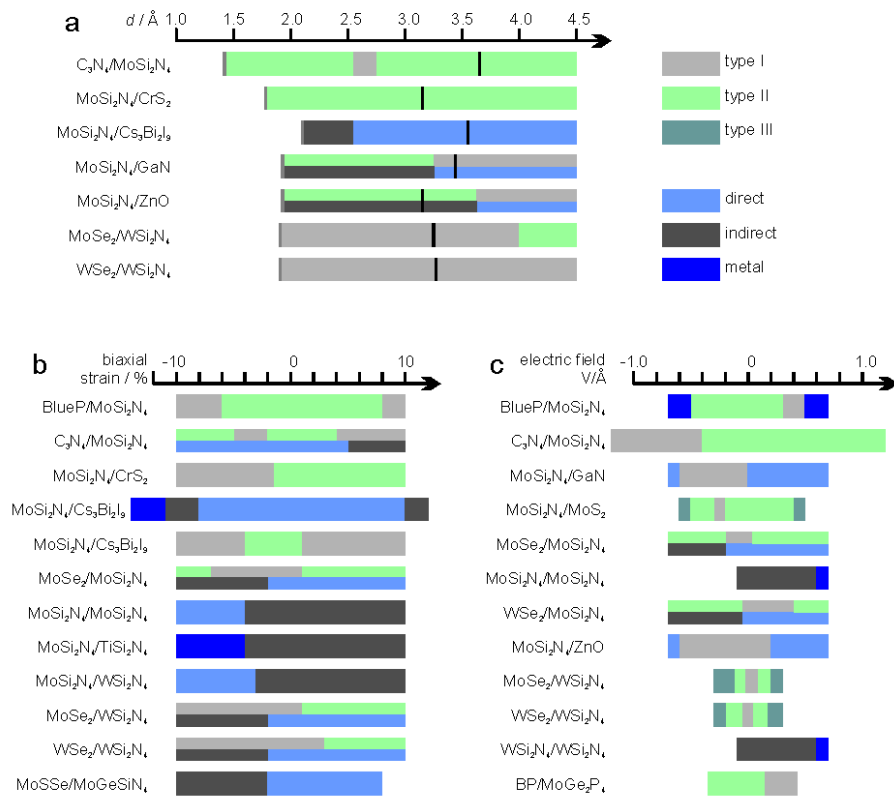
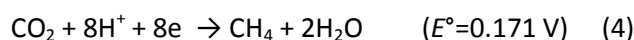
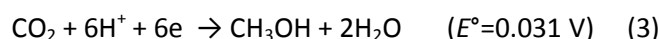
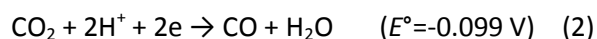


Fig. S3. Type of MA_2Z_4 -heterostructure as a function of **a**, vertical stress (interlayer distance), **b**, biaxial strain and **c**, electric field according to the data shown in **Table S2**. In **a**, the black vertical lines indicate the positions of the interlayer distance without vertical stress. The gray vertical lines indicate the positions of the minimal interlayer distance given by the sum of the covalent radii.

3. Catalytic properties of MA₂Z₄ materials

Reaction potential depends on pH as defined by the Nernst equation: $E^{\circ}(\text{pH}) = E^{\circ}(\text{pH}=0) + \text{pH} \cdot 0.059$ eV, (at 25° C). The band edges of a semiconductor can be evaluated either directly from its energy bands distribution, or from its bandgap E_g alone by using the following equations [42] (Liu2011APL): $E_{\text{VBE}} = x - 4.5\text{eV} + 0.5E_g$, and $E_{\text{CBE}} = E_{\text{VBE}} - E_g$, where x is the geometric average value of the electronegativity of the constituent atoms ($x = 5.195$ for MoSi₂N₄ [43] (Bartolotti1980JACS)), and 4.5 eV is the energy of free electrons on the hydrogen scale.

The water splitting reaction $\text{H}_2\text{O} \rightarrow \text{H}_2 + 1/2\text{O}_2$ consists of two half-reactions [44] (Nishioka2023NatRevMethods): hydrogen evolution reaction (HER) $2\text{H}^+ + 2\text{e}^- \rightarrow \text{H}_2$ and oxygen evolution reaction (OER) $\text{H}_2\text{O} + 2\text{h}^+ \rightarrow 1/2\text{O}_2 + 2\text{H}^+$. Thus, the catalyst's VBE should be lower than the potential of the OER ($E(\text{H}_2\text{O}/\text{O}_2) = -5.67$ eV + pH·0.059 eV), its CBE should be higher than the potential of HER ($E(\text{H}^+/\text{H}_2) = -4.44$ eV + pH·0.059 eV), with the minimal energy gap of 1.23 eV. Photocatalytic CO₂ reduction reaction can be realized by one of the following reactions:



The potentials E° shown here (vs standard hydrogen electrode (SHE) at pH=0) were calculated using the free energy [45] (Latimer_book). The positions of the potentials for water splitting and CO₂ reduction reactions, together with the band edges of a hypothetically suitable catalyst are shown in Fig. 7a.

Table S3. Catalytic properties of MA₂Z₄ materials. BT - bandgap type (d - direct, i - indirect), x - the geometric average of the electronegativity of the constituent atoms. WS - photo-catalytic water splitting, CO₂ - CO₂ reduction reactions, where "1,2,3,4" is the reaction number as defined above, α - absorption coefficient, given for visible light range: 1.59 - 3.26 eV (780 - 380nm). ML - monolayer, SAC - single atom catalyst, and H - hetero-structures.

composition	BT	E_g / eV PBE	E_g / eV HSE	x	E_{CBM} / eV NHE	E_{VBM} / eV NHE	WS	CO ₂	α 10 ⁵ cm ⁻¹	strain biaxial	reference
ML											
CrSi ₂ N ₄	i	0.49	0.99	NA	0.86	1.85	no	no	NA	NA	[46]
HfSi ₂ N ₄	i,d	1.77(i)	2.84(d)	NA	-0.14	2.7	yes	2,3,4	0.3-1.8	NA	[46]
MoGe ₂ N ₄	i	0.85	1.42	NA	0.61	2.03	no	no	0.6-4.0	NA	[46]
2H-MoGe ₂ N ₄	i	0.91	1.27	NA	0.46	1.86	no	no	0.3-2.0		[47]
MoSi ₂ N ₄	i	1.72	2.21	NA	0.28	2.49	no	no	NA	NA	[46]
MoSi ₂ N ₄	i	1.38	2.13	NA	-1.06	1.11	no	no	NA	$\epsilon=2\%$ shifts band edges to CBM=-4.12(-0.32)eV and VBM=-5.85(1.41)eV so that WS and CO ₂ reduction (1,2,3,4) are possible	[48]
2H-MoSi ₂ N ₄	i	1.79	2.23	NA	-0.64	1.66	yes	1,2,3,4	0.2-2.9		[47]
TiSi ₂ N ₄	i	1.61	2.74	NA	-0.12	2.62	yes	2,3,4	NA	NA	[46]

WGe ₂ N ₄	i	1.18	1.6	NA	0.61	2.21	no	no	NA	NA	[46]
2H-WGe ₂ N ₄	i,d	1.15(i)	1.51(d)	NA	-0.14	1.41	yes	2,3,4	0.2-1.7		[47]
WSi ₂ N ₄	i	2.19	2.51	NA	0.19	2.7	no	no	NA	NA	[46]
WSi ₂ N ₄	NA	1.65	2.38	NA	-1.47	0.92	no	no	NA	$\epsilon \approx 3\%$ shifts band edges to: CBM=-4.09(-0.35)eV and VBM=-5.76(1.32)eV $\epsilon \approx 4\%$ shifts band edges to: CBM=-4.439(-0.01)eV and VBM=-5.91(1.47)eV so that WS and CO ₂ reduction (1,2,3,4) are possible	[48]
2H-WSi ₂ N ₄	i	2.07	2.57	NA	-1.04	1.26	yes	1,2,3,4	0.2-0.6		[47]
ZrSi ₂ N ₄	i,d	1.56(i)	2.78(d)	NA	-0.08	2.7	yes	3,4	NA	NA	[46]
ML, Janus											
MoSi ₂ N ₄	i	NA	2.32	NA	-0.81	1.51	yes	1,2,3,4	0.1-0.6	uniaxial: both band edges position increase as a function of ϵ (ϵ increasing, band edges decreasing)	[49]
MoSiGeN ₄	i	NA	1.81	NA	-0.55	1.86	yes	1,2,3,4	0.1-3.6	uniaxial: both band edges position increase as a function of ϵ (ϵ increasing, band edges decreasing)	[49]
WSiGeN ₄	i	NA	2.25	NA	-1.28	1.56	yes	1,2,3,4	0.1-0.6	uniaxial: both band edges position increase as a function of ϵ (ϵ increasing, band edges decreasing)	[49]
ML, strain											
MoSi ₂ N ₄	i	1.96	NA	NA	-0.71	1.42	yes	1,2,3,4	0-0.2		[50]
MoSi ₂ N ₄ $\epsilon \approx 6\%$	i	0.91	NA	NA	NA	NA	no	no	0.5-5.0	$\epsilon \approx 6\%$ shifts abs spectrum by 100 nm to longer wavelength	[50]
MoSi ₂ N ₄ $\epsilon \approx -6\%$	i	2.76	NA	NA	-1.32	1.88	yes	1,2,3,4	0-3.0	$\epsilon \approx -6\%$ shifts abs spectrum by 100 nm to shorter wavelength	[50]
SAC											
MoSi ₂ N ₄	i	1.89	NA	5.195	-0.250	1.640	yes	1,2,3,4	0.2-3.0	NA	[51]
1Au	i	1.81	NA	NA	-0.210	1.600	yes	1,2,3,4	0.4-3.1	NA	[51]
2Au	i	1.78	NA	NA	-0.195	1.585	yes	1,2,3,4	NA	NA	[51]
3Au	i	1.42	NA	NA	-0.015	1.405	yes	3,4	0.4-3.4	NA	[51]
5Au	i	0.2	NA	NA	0.595	0.795	no	no	NA	NA	[51]
7Au	i	0.07	NA	NA	0.660	0.730	no	no	0.06-0.51	NA	[51]
9Au	i	0	NA	NA	0.695	0.695	no	no	0.18-0.57	NA	[51]
SAC											
MoSi ₂ N ₄	i	1.89	NA	5.195	-0.25	1.64	yes	1,2,3,4	0.02-0.34	NA	[52]
1Li	i	1.73	NA	5.139	-0.226	1.504	yes	1,2,3,4	0.57-0.92	NA	[52]
2Li	i	1.58	NA	5.085	-0.205	1.375	yes	1,2,3,4	NA	NA	[52]
3Li	i	1.42	NA	5.033	-0.177	1.243	yes	2,3,4	NA	NA	[52]
1Na	i	1.61	NA	5.13	-0.175	1.435	yes	2,3,4	1.09-1.34	NA	[52]
2Na	i	1.53	NA	5.068	-0.197	1.333	yes	1,2,3,4	NA	NA	[52]
3Na	i	1.46	NA	5.008	-0.222	1.238	yes	1,2,3,4	NA	NA	[52]
1K	i	1.75	NA	5.115	-0.26	1.49	yes	1,2,3,4	0.89-1.14	NA	[52]
2K	i	1.69	NA	5.039	-0.306	1.384	yes	1,2,3,4	NA	NA	[52]
3K	i	1.47	NA	4.966	-0.269	1.201	yes	1,2,3,4	NA	NA	[52]
H											
MoSi ₂ N ₄	i	1.78	2.36	NA	-0.82	1.54	yes	1,2,3,4	0.16-0.8	NA	[19]
BlueP	i	1.94	2.76	NA	-0.46	2.3	yes	1,2,3,4	0.14-0.5	NA	[19]
MoSi ₂ N ₄ /BlueP	i	1.175	2	NA	-0.71	1.63	yes	1,2,3,4	0.16-2.0	$\epsilon \approx 0$ to (+6%) shifts absorption spectrum by 0 to (-1)eV; $\epsilon \approx -0$ to (-8%) by 0 to (+1eV)	[19]
SAC											
MoSi ₂ N ₄	i	1.78	2.31	NA	-0.77	1.58	yes	1,2,3,4	0-1.0	NA	[53]
AB BL MoSi ₂ N ₄	i	1.7	2.23	NA	-0.7	1.23	yes	1,2,3,4	0-3.5		[53]
SAC											
2H-MoSi ₂ N ₄ /MoS ₂	i	NA	2.08	NA	NA	NA	yes	1,2,3,4	NA	NA	[29]
2H'-MoSi ₂ N ₄ /MoS ₂	i	NA	1.93	NA	NA	NA	yes	1,2,3,4	NA	NA	[29]
2H-MoSi ₂ N ₄ /MoSSe	i	NA	1.26	NA	NA	NA	no	no	NA	NA	[29]
2H'-MoSi ₂ N ₄ /MoSSe	i	NA	1.55	NA	NA	NA	no	no	NA	NA	[29]
SAC											
WSe ₂ /MoSi ₂ N ₄	i, II	1.38	1.81	NA	-0.48	1.33	yes	1,2,3,4	0.3-2.2	NA	[33]
InSe/MoSi ₂ N ₄	d, II	1.35	1.61(GGA-1/2)	NA	-0.18	1.43	yes	2,3,4	0-1.5	NA	[26]

C ₂ N/MoSi ₂ N ₄	d, II	NA	1.74	NA	-0.2	1.54	yes	1,2,3,4	0-4	NA	[20]
MoSi ₂ N ₄ /CrS ₂	i, II	0.99	1.52	NA	NA	NA	yes	NA	NA		[23]
WSi ₂ N ₄ /MoSi ₂ N ₄	i, II	NA	1.9	NA	-0.69	1.3	yes	NA	0.2-3.2	NA	[35]
(MoSi ₂ N ₄) ₅ / (MoSiGeN ₄) ₀		1.925	2.385	NA	-5.463	1.660	yes	1,2,3,4	0-0.35	NA	[39]
(MoSi ₂ N ₄) ₄ / (MoSiGeN ₄) ₁		1.823	2.71	NA	NA	NA	yes	1,2,3,4	NA	NA	[39]
(MoSi ₂ N ₄) ₃ / (MoSiGeN ₄) ₂		1.716	2.137	NA	NA	NA	yes	1,2,3,4	NA	NA	[39]
(MoSi ₂ N ₄) ₂ / (MoSiGeN ₄) ₃		1.598	2.021	NA	NA	NA	yes	2,3,4	0-0.35	NA	[39]
(MoSi ₂ N ₄) ₁ / (MoSiGeN ₄) ₄		1.494	1.979	NA	NA	NA	yes	3,4	NA	NA	[39]

References

1. Wang, L., et al., *Intercalated architecture of MA₂Z₄ family layered van der Waals materials with emerging topological, magnetic and superconducting properties*. Nature Communications, 2021. **12**(1): p. 2361.
2. Simmons, *Generalized formula for the electric tunnel effect between similar electrodes separated by a thin insulating film*. Journal of Applied Physics, 1963. **34**(6): p. 1793–1803.
3. Matthews, N., M.J. Hagmann, and A. Mayer, *Comment: "Generalized formula for the electric tunnel effect between similar electrodes separated by a thin insulating film" [J. Appl. Phys. 34, 1793 (1963)]*. Journal of Applied Physics, 2018. **123**(13): p. 136101.
4. Liang, Q., et al., *Modulation of Schottky barrier in XSi₂N₄/graphene (X = Mo and W) heterojunctions by biaxial strain*. Chinese Physics B, 2022. **31**(8): p. 087101.
5. Cao, L., et al., *Two-dimensional van der Waals electrical contact to monolayer MoSi₂N₄*. Applied Physics Letters, 2021. **118**(1): p. 013106.
6. Pham, D.K., *Electronic properties of a two-dimensional van der Waals MoGe₂N₄/MoSi₂N₄ heterobilayer: effect of the insertion of a graphene layer and interlayer coupling*. RSC Advances, 2021. **11**(46): p. 28659–28666.
7. Liang, Q., et al., *Van der Waals stacking-induced efficient Ohmic contacts and the weak Fermi level pinning effect in MoSi₂N₄ and WSi₂N₄ contact with two-dimensional metals*. Physica E: Low-dimensional Systems and Nanostructures, 2023. **149**: p. 115686.
8. Li, Z.H., et al., *Graphene/MoSi₂X₄: A class of van der Waals heterojunctions with unique mechanical and optical properties and controllable electrical contacts*. Applied Surface Science, 2023. **614**: p. 156095.
9. Yuan, G., et al., *Highly sensitive band alignment of the graphene/MoSi₂N₄ heterojunction via an external electric field*. ACS Applied Electronic Materials, 2022. **4**(6): p. 2897–2905.
10. Wang, Q., et al., *Efficient Ohmic contacts and built-in atomic sublayer protection in MoSi₂N₄ and WSi₂N₄ monolayers*. npj 2D Materials and Applications, 2021. **5**(1): p. 71.
11. Tho, C.C., et al., *Cataloguing MoSi₂N₄ and WSi₂N₄ van der Waals heterostructures: An exceptional material platform for excitonic solar cell applications*. Advanced Materials Interfaces, 2023. **10**(2): p. 2201856.
12. He, X., et al., *Achieving real Ohmic contact by the dual protection of outer layer atoms and surface functionalization in 2D metal MXenes/MoSi₂N₄ heterostructures*. Journal of Materials Chemistry C, 2023. **11**(14): p. 4728–4741.
13. Nguyen, C.V., et al., *Two-dimensional metal/semiconductor contact in a Janus MoSH/MoSi₂N₄ van der Waals heterostructure*. The Journal of Physical Chemistry Letters, 2022. **13**(11): p. 2576–2582.
14. Zhang, X., et al., *Ohmic contacts in MXene/MoSi₂N₄ heterojunctions*. Applied Physics Letters, 2023. **123**(2): p. 023505.

15. Ma, X., et al., *Tunable Schottky barrier of WSi_2N_4 /graphene heterostructure via interface distance and external electric field*. Applied Surface Science, 2023. **615**: p. 156385.
16. Binh, N.T.T., et al., *Interfacial electronic properties and tunable contact types in graphene/Janus $MoGeSiN_4$ heterostructures*. The Journal of Physical Chemistry Letters, 2021. **12**(16): p. 3934–3940.
17. Shu, Y., et al., *Efficient Ohmic contact in monolayer CrX_2N_4 ($X = C, Si$) based field-effect transistors*. Advanced Electronic Materials, 2023. **9**(3): p. 2201056.
18. Fang, L., et al., *First-principles insights of electronic properties of Blue Phosphorus/ $MoSi_2N_4$ van der Waals heterostructure via vertical electric field and biaxial strain*. Physica E: Low-dimensional Systems and Nanostructures, 2022. **143**: p. 115321.
19. Xuefeng, C., et al., *A direct Z-scheme $MoSi_2N_4$ /BlueP vdW heterostructure for photocatalytic overall water splitting*. Journal of Physics D: Applied Physics, 2022. **55**(21): p. 215502.
20. Zeng, J., et al., *Boosting the photocatalytic hydrogen evolution performance of monolayer C_2N coupled with $MoSi_2N_4$: density-functional theory calculations*. Physical Chemistry Chemical Physics, 2021. **23**(14): p. 8318–8325.
21. Nguyen, C.Q., et al., *Tunable type-II band alignment and electronic structure of C_3N_4 / $MoSi_2N_4$ heterostructure: Interlayer coupling and electric field*. Physical Review B, 2022. **105**(4): p. 045303.
22. Zhao, J., et al., *Spin-valley coupling and valley splitting in the $MoSi_2N_4$ / $CrCl_3$ van der Waals heterostructure*. Applied Physics Letters, 2021. **119**(21): p. 213101.
23. Li, R.-X., et al., *$MoSi_2N_4$ / CrS_2 van der Waals heterostructure with high solar-to-hydrogen efficiency*. Physica E: Low-dimensional Systems and Nanostructures, 2022. **144**: p. 115443.
24. Liu, C., et al., *Effect of vertical strain and in-plane biaxial strain on type-II $MoSi_2N_4$ / $Cs_3Bi_2I_9$ van der Waals heterostructure*. Journal of Applied Physics, 2022. **131**(16): p. 163102.
25. Ng, J.Q., et al., *Tunable electronic properties and band alignments of $MoSi_2N_4$ / GaN and $MoSi_2N_4$ / ZnO van der Waals heterostructures*. Applied Physics Letters, 2022. **120**(10): p. 103101.
26. He, Y., et al., *High hydrogen production in the $InSe$ / $MoSi_2N_4$ van der Waals heterostructure for overall water splitting*. Physical Chemistry Chemical Physics, 2022. **24**(4): p. 2110–2117.
27. Xu, X., et al., *Type-II $MoSi_2N_4$ / MoS_2 van der Waals heterostructure with excellent optoelectronic performance and tunable electronic properties*. The Journal of Physical Chemistry C, 2023. **127**(16): p. 7878–7886.
28. Bafekry, A., et al., *A van der Waals heterostructure of MoS_2 / $MoSi_2N_4$: a first-principles study*. New Journal of Chemistry, 2021. **45**(18): p. 8291–8296.
29. Jalil, A., et al., *Prediction of direct Z-scheme H and \dot{H} -phase of $MoSi_2N_4$ / $MoSX$ ($X = S, Se$) van der Waals heterostructures: A promising candidate for photocatalysis*. Chemical Engineering Journal, 2023. **470**: p. 144239.
30. Cai, X., et al., *A two-dimensional $MoSe_2$ / $MoSi_2N_4$ van der Waals heterostructure with high carrier mobility and diversified regulation of its electronic properties*. Journal of Materials Chemistry C, 2021. **9**(31): p. 10073–10083.
31. Wu, Q., et al., *Semiconductor-to-metal transition in bilayer $MoSi_2N_4$ and WSi_2N_4 with strain and electric field*. Applied Physics Letters, 2021. **118**(11): p. 113102.
32. Hussain, G., et al., *Strain modulated electronic and optical properties of laterally stitched $MoSi_2N_4$ / XSi_2N_4 ($X=W, Ti$) 2D heterostructures*. Physica E: Low-dimensional Systems and Nanostructures, 2022. **144**: p. 115471.
33. Liu, Y., et al., *2D WSe_2 / $MoSi_2N_4$ type-II heterojunction with improved carrier separation and recombination for photocatalytic water splitting*. Applied Surface Science, 2023. **611**: p. 155674.
34. Cai, X., et al., *Indirect to direct bandgap transition and enhanced optoelectronic properties in WSe_2 monolayer through forming WSe_2 / $MoSi_2N_4$ bilayer*. Social Science Research Network, 2021.

35. Zhao, P., et al., *Theoretical study of a novel $WSi_2N_4/MoSi_2N_4$ heterostructure with ultrafast carrier transport*. The Journal of Physical Chemistry C, 2022. **126**(27): p. 11380–11388.
36. Pei, M., et al., *Tuning the band alignment and electronic properties of XSe_2/WSi_2N_4 ($X=Mo,W$) van der waals heterostructures with high carrier mobility*. Physica E: Low-dimensional Systems and Nanostructures, 2023. **149**: p. 115656.
37. Guo, Y., et al., *Two-dimensional type-II $BP/MoSi_2P_4$ vdW heterostructures for high-performance solar cells*. The Journal of Physical Chemistry C, 2022. **126**(9): p. 4677–4683.
38. Nguyen, C., et al., *Two-dimensional Boron Phosphide/ $MoGe_2N_4$ van der Waals heterostructure: A promising tunable optoelectronic material*. The Journal of Physical Chemistry Letters, 2021. **12**(21): p. 5076–5084.
39. Mwankemwa, N., et al., *First principles calculations investigation of optoelectronic properties and photocatalytic CO_2 reduction of $(MoSi_2N_4)_5-n/(MoSiGeN_4)_n$ in-plane heterostructures*. Results in Physics, 2022. **37**: p. 105549.
40. Wang, J., et al., *Manipulable electronic and optical properties of two-dimensional $MoTe/MoGe_2N_4$ van der Waals heterostructures*. Nanomaterials, 2021. **11**(12): p. 3338.
41. Zhang, Q.-K., et al., *2D Janus $MoSSe/MoGeSiN_4$ vdW heterostructures for photovoltaic and photocatalysis applications*. Journal of Alloys and Compounds, 2023. **938**: p. 168708.
42. Liu, J.J., et al., *Electronic structure and optical properties of Ag_3PO_4 photocatalyst calculated by hybrid density functional method*. Applied Physics Letters, 2011. **99**(19): p. 191903.
43. Bartolotti, L.J., S.R. Gadre, and R.G. Parr, *Electronegativities of the elements from simple Xa theory*. Journal of the American Chemical Society, 1980. **102**(9): p. 2945–2948.
44. Nishioka, S., et al., *Photocatalytic water splitting*. Nature Reviews Methods Primers, 2023. **3**(1): p. 42.
45. Latimer, W.M., *Oxidation Potentials*. 1952, New York: Prentice Hall.
46. Yadav, A., et al., *Novel two-dimensional MA_2N_4 materials for photovoltaic and spintronic applications*. The Journal of Physical Chemistry Letters, 2021. **12**(41): p. 10120–10127.
47. Mortazavi, B., et al., *Exceptional piezoelectricity, high thermal conductivity and stiffness and promising photocatalysis in two-dimensional $MoSi_2N_4$ family confirmed by first-principles*. Nano Energy, 2021. **82**: p. 105716.
48. Chen, J. and Q. Tang, *The versatile electronic, magnetic and photo-electro catalytic activity of a new 2D MA_2Z_4 family***. Chemistry – A European Journal, 2021. **27**(38): p. 9925–9933.
49. Yu, Y., et al., *Novel two-dimensional Janus $MoSiGeN_4$ and $WSiGeN_4$ as highly efficient photocatalysts for spontaneous overall water splitting*. ACS Applied Materials & Interfaces, 2021. **13**(24): p. 28090–28097.
50. Jian, C.-c., et al., *Strained $MoSi_2N_4$ monolayers with excellent solar energy absorption and carrier transport properties*. The Journal of Physical Chemistry C, 2021. **125**(28): p. 15185–15193.
51. Xu, J., et al., *First-principles investigations of electronic, optical, and photocatalytic properties of Au-adsorbed $MoSi_2N_4$ monolayer*. Journal of Physics and Chemistry of Solids, 2022. **162**: p. 110494.
52. Sun, Z., et al., *Alkali-metal(Li, Na, and K)-adsorbed $MoSi_2N_4$ monolayer: an investigation of its outstanding electronic, optical, and photocatalytic properties*. Communications in Theoretical Physics, 2022. **74**(1): p. 015503.
53. Zhao, J., et al., *Stacking engineering: A boosting strategy for 2D photocatalysts*. The Journal of Physical Chemistry Letters, 2021. **12**(41): p. 10190–10196.